Dalton Transactions

PAPER

Copper(II) complex with a redox-noninnocent Schiff base bearing a tetraphenyldisiloxane unit: synthesis, structure and catalytic oxidation of cyclohexane†

Christopher Wittmann,[a] Oleg Palamarciuc,[b,c] Mihaela Dascalu,[b] Maria Cazacu [iD] [b]
Dmytro S. Nesterov, [iD] *[d,e] Armando J. L. Pombeiro, [iD] *[e] Peter Rapta [iD] *[f] and
Vladimir B. Arion [iD] *[a,b]

An organic−inorganic diamine, 1,3-bis(aminopropyl)tetraphenyldisiloxane, was prepared and introduced as a flexible spacer into the structure of a salen-type Schiff base (H_2L^7) extending the available small library of similar compounds derived from 1,3-bis(aminopropyl)tetramethyldisiloxane and substituted 2-hydroxybenzaldehydes (H_2L^1–H_2L^6). Like the previously reported mononuclear copper(II) complexes $[CuL^1]$–$[CuL^6]$, the new copper(II) complex $[CuL^7]$, obtained by reaction of $Cu(OAc)_2 \cdot H_2O$ with H_2L^7 in a mixture of organic solvents, has a tetrahedrally distorted square-planar (N_2O_2) coordination geometry. X-ray crystallography has shown that compared to $[CuL^1]$–$[CuL^6]$ the Si−O−Si angle in $[CuL^7]$ is even closer to linear due to stronger intramolecular interactions between Ph groups than between Me groups in the central−R_2Si−O−SiR_2− fragment (R = Ph and Me, respectively). $[CuL^7]$ can be electrochemically reversibly oxidised by two successive one-electron processes, generating stable phenoxyl mono- and diradicals. Both oxidations are ligand-centred, leading to the formation of coordinated phenoxyl radicals. The UV spectrum of $[CuL^7]$ consists of $\pi \rightarrow \pi^\star$ and LMCT $\sigma \rightarrow d$ transitions. The low-energy d−d absorption is well described by AILFT CAS(9,5)/NEVPT2 calculations. The one-electron oxidised compound $[CuL^7]^+$ should exist in the triplet ground state as $^3[CuL^7]^+$ with one unpaired electron located on the $d_{x^2-y^2}$ orbital of copper(II) (d^9, $S_{Cu} = \frac{1}{2}$) and another electron on the molecular orbital (MO) comprising p_z oxygen and carbon atoms of the phenoxyl radical ($S_{rad} = \frac{1}{2}$). The broad absorption in the vis-NIR region of the optical spectrum of the one-electron oxidised complex is due to intervalence charge transfer in the triplet species $^3[CuL^7]^+$, but not in the $[CuL^7]^{2+}$ one. The doubly oxidised $[CuL^7]$ species shows very close doublet and quartet states, where the doublet state has an unpaired electron located on the Cu(II) d-orbital, while the quartet state has one unpaired electron on the Cu(II) d-orbital and two unpaired electrons on π-bonding orbitals. In all state-averaged CASSCF cases, the occupation of the Cu(II) d-orbital is nearly 1.0, indicating its limited involvement in the excited states. Catalytic studies showed that $[CuL^7]$ acts as a catalyst for the oxidation of alkanes with peroxides under very unusual solvent-free conditions, converting cyclohexane into cyclohexanol and cyclohexanone (with hydrogen peroxide or *tert*-butyl hydroperoxide as the oxidant) or into cyclohexanol and ε-caprolactone (with *m*-chloroperoxybenzoic acid as the oxidant). Theoretical investigations of the catalytic reaction mechanisms disclosed the principal intermediates.

[a]*University of Vienna, Institute of Inorganic Chemistry, Währinger Strasse 42, 1090 Vienna, Austria*
[b]*Inorganic Polymers Department, "Petru Poni" Institute of Macromolecular Chemistry, Aleea Gr. Ghica Voda 41 A, Iasi 700487, Romania. E-mail: vladimir.arion@univie.ac.at*
[c]*Physics of Semiconductors and Devices Laboratory, Faculty of Physics and Engineering and Institute of Applied Physics, Moldova State University, MD-2009, Chişinău, Republic of Moldova*
[d]*Centro de Estudos de Engenharia Química, Instituto Superior de Engenharia de Lisboa, Instituto Politécnico de Lisboa, R. Conselheiro Emídio Navarro, 1, 1959-007 Lisboa, Portugal*
[e]*Centro de Química Estrutural, Institute of Molecular Sciences, Instituto Superior Técnico, Universidade de Lisboa, Av. Rovisco Pais, 1049-001 Lisboa, Portugal.*

E-mail: dmytro.nesterov@vis.isel.pt, dmytro.nesterov@tecnico.ulisboa.pt, pombeiro@tecnico.ulisboa.pt

[f]*Institute of Physical Chemistry and Chemical Physics, Faculty of Chemical and Food Technology, Slovak University of Technology in Bratislava, Radlinského 9, SK-81237 Bratislava, Slovak Republic. E-mail: peter.rapta@stuba.sk*

†Electronic supplementary information (ESI) available: Experimental details; synthesis of 1,3-bis(aminopropyl)tetraphenyldisiloxane; tables and figures with structural, spectroscopic (NMR and UV–vis) and mass spectrometry details; theoretical calculations; and catalytic data. CCDC 2413535 and 2413536. For ESI and crystallographic data in CIF or other electronic format see DOI: https://doi.org/10.1039/d5dt01028d

Introduction

Recently, we reported that 2-hydroxybenzaldehyde and related derivatives react with 1,3-bis(3-aminopropyl)tetramethyldisiloxane in the presence of Ni(II), Cu(II) or Zn(II) in a 2:1:1 molar ratio with the formation of tetrahedrally distorted square-planar metal(II) complexes of tetradentate Schiff bases with a *trans*-arrangement of N_2O_2 donor atoms.[1–6] The most interesting feature is the formation of a 12-membered central chelate ring including the tetramethyldisiloxane unit, which separates the aliphatic chains, significantly diminishing the mechanical strain in the emerging chelate ring. This was called a "shoulder yoke effect".

In addition to basic research interest, the reported metal complexes with open-chain and macrocyclic Schiff bases have found application in catalysis. Some of the potential candidates for such catalysts are polynuclear or mononuclear Cu(II) complexes with tetramethyldisiloxane-spaced hexadentate macrocyclic ligands or potentially tridentate or tetradentate Schiff bases bearing trimethylsilane units, as shown in Chart 1. Oxidation of cyclohexane with H_2O_2 in acetonitrile/water (ACN/H_2O) in the presence of tetranuclear copper(II) complexes with macrocyclic (**I**) and open-chain (**II**) disiloxane-spaced ligands afforded 8% total product yield after *ca.* 30 min.[7] Addition of trifluoroacetic acid (TFA) improved the catalytic performance of the complexes by increasing the total product yield to 14% after *ca.* 1 h. Cu(II) complexes of type **III**, especially those with electron-withdrawing substituents, such as chloro, bromo and nitro on the aromatic ring, showed high catalytic activity in the aerobic oxidation of benzyl alcohol to
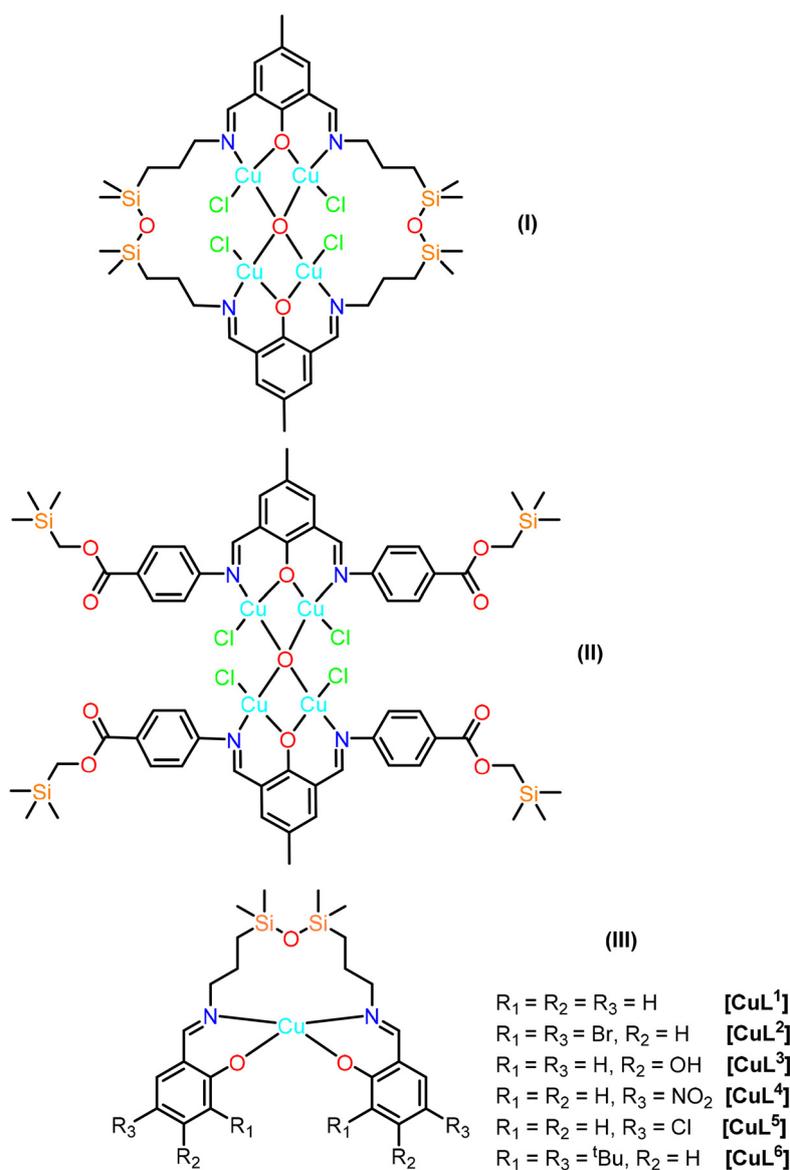

$R_1 = R_2 = R_3 = H$	**[CuL¹]**
$R_1 = R_3 = Br, R_2 = H$	**[CuL²]**
$R_1 = R_3 = H, R_2 = OH$	**[CuL³]**
$R_1 = R_2 = H, R_3 = NO_2$	**[CuL⁴]**
$R_1 = R_2 = H, R_3 = Cl$	**[CuL⁵]**
$R_1 = R_3 = {}^tBu, R_2 = H$	**[CuL⁶]**

Chart 1 Line drawings of Cu(II) complexes with macrocyclic and open-chain Schiff bases derived from tetramethyldisiloxane-containing diamines, 2,6-diformyl-4-methylphenol and substituted 2-hydroxybenzaldehydes.

benzaldehyde, mediated by the TEMPO radical, under mild conditions in the presence of K_2CO_3 as a base with overall yields and TONs up to 99% and 990, respectively.[2] A tetranuclear Zn(II) complex with four Schiff base entities built on an oligomeric silsesquioxane (known as POSS) core was reported recently to act as an effective catalyst in the cycloaddition reactions of CO_2 with terminal alkyl and aryl epoxides under mild conditions, while tolerating different functionalities including halide and ether groups.[8]

The flexible siloxane unit confers specific features to these Schiff bases, such as low intermolecular forces, low surface free energy, large free volume, good thermal, oxidative and UV–vis stability, good environmental compatibility and biocompatibility. One critical issue is associated with the requirement for efficient catalyst recycling. Recycling of the catalysts is essential for a practical and cost-effective implementation. A possible approach to resolve this problem is the application of a heterogeneous catalyst (a MOF or coordination polymer resistant to the operating conditions) that is totally insoluble in the reaction mixture (usually, an ACN or ACN/H_2O mixture).

Another strategy suggests the use of a hydrophobic catalyst, which is predicted to be selectively soluble in apolar alkane substrates (*e.g.*, cyclohexane), but insoluble in the liquid polar oxidation products of alkanes (*e.g.* cyclohexanol and cyclohexanone). In this case, no solvent is required (that is very attractive from the ecological point of view), and the catalyst might be

precipitated and easily separated for recycling after the formation of the reaction products. In this context, we aimed (i) to replace the tetramethyldisiloxane unit by a more lipophilic disiloxane unit, (ii) to prepare a Schiff base and a copper(II) complex, (iii) to study the influence of this new unit on complex formation, and its structure, stability, lipophilicity and solubility in apolar solvents, (iv) to investigate whether the complex exhibits noninnocent behaviour[9–14] and (v) to evaluate its potential to act as a catalyst in the oxidation of cyclohexane in the absence of other solvents. While the aerobic solvent-free oxidation of cyclohexane is a common subject of investigation, the respective solvent-free oxidations with organic peroxides are much less studied and, moreover, there is a lack of knowledge about the behaviour and catalytic decomposition of organic oxidants under such conditions.

Herein, we report on the multistep synthesis and the spectroscopic and structural characterisation of the Schiff base, H_2L^7, derived from 3,5-di-*tert*-butyl-2-hydroxybenzaldehyde and 1,3-bis-(3-aminopropyl)tetraphenyldisiloxane, as well as its Cu(II) complex **[CuL^7]** (see Scheme 1). The noninnocent behaviour of **[CuL^7]** was disclosed by electrochemical and spectroelectrochemical measurements and supported by DFT and CASSCF calculations. The application of the complex with a redox-active ligand as a catalyst in the oxidation of cyclohexane in the very unusual absence of any other solvent (by taking advantage of the solubility of the complex in the alkane sub-
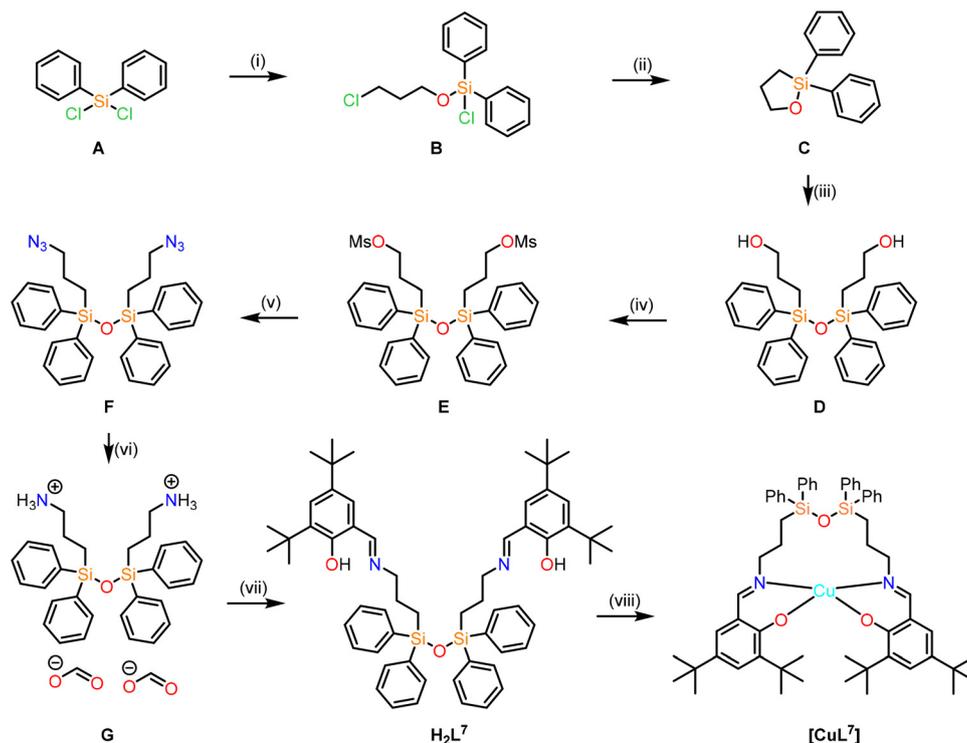
Scheme 1 Synthetic pathway to H_2L^7 and **[Cu^{II}L^7]**. Reagents and conditions: (i) 3-chloropropan-1-ol, DIPEA, THF$_{dry}$, dry toluene, 0 °C to room temperature, 4.5 h; (ii) Na^0, dry toluene, 125 °C, 5 h; (iii) 1 M HCl, water, dioxane, 100 °C, 1.5 h; (iv) MsCl, DCM$_{dry}$, TEA, 0 °C to room temperature, 2 h; (v) NaN$_3$, DMF, water, 90 °C, 2 h; (vi) Pd/C 10%, H_2 4 bar, THF$_{dry}$, 4 h; (vii) 3,5-di-*tert*-butyl-2-hydroxybenzaldehyde, methanol, reflux, 3 h; (viii) Cu(OAc)$_2$·H_2O, MeOH/CHCl$_3$, reflux, 30 min.

strate) was disclosed. The effect of the oxidant on the degree of cyclohexane oxidation and thus on the types of obtained oxidised products was also investigated. The key intermediates of the catalytic reactions were studied using DFT calculations.

Results and discussion

Synthesis of H_2L^7 and $[CuL^7]$

The synthesis of H_2L^7 was performed in seven chemical steps, as shown in Scheme 1. The synthesis of H_2L^7 started from diphenyldichlorosilane (**A**) by reaction with 3-chloropropan-1-ol in the presence of N,N-diisopropylethylamine (DIPEA) as a base in dry toluene to afford 3-chloropropoxydiphenylsilyl chloride (**B**) in 88% yield. Further reaction of species **B** with Na[0] in dry boiling toluene resulted in the formation of 1,1-diphenyl-1-sila-2-oxacyclopentane (**C**) in 27% yield. In the next step, species **C** was hydrolysed in boiling dioxane by addition of water and a small amount of 1 M HCl to give the crude diol **D** in 90% yield. The structure of the diol was confirmed by X-ray crystallography and is shown in Fig. S1 in the ESI.†

Species **D** was then converted into dimesylate **E** in 72% yield by reaction with mesyl chloride in DCM, in the presence of triethylamine. Thereafter, the quantitative reaction of species **E** with sodium azide in DMF upon heating led to the formation of diazido species **F**, which was then catalytically reduced with H_2 in the presence of Pd/C to a diamine and isolated as a crude lyophilisate of diammonium formate salt **G**. Purification of this species on reverse-phase HPLC was required to give a white cloudy solid in 31% yield. The condensation reaction of the pure product **G** with 3,5-di-*tert*-butyl-2-hydroxybenzaldehyde in a 1 : 2 molar ratio in methanol in the presence of triethylamine afforded the Schiff base H_2L^7 (Scheme 1) in 83% yield. The number of resonances in the ^{1}H, ^{13}C, and ^{29}Si NMR spectra of species **G** and Schiff base H_2L^7 in DMSO-d_6 (see Fig. S2–S7†) was in accordance with the two-fold symmetry of the molecule in solution. The ESI mass spectra of species **C**, **D**, **E** and **G** are shown in Fig. S8–S12.† The positive-ion ESI mass spectrum of H_2L^7 showed a strong peak with m/z 929.62 (Fig. S13†) attributed to the $[M + H^+]^+$ ion. The reaction of H_2L^7 with $Cu(OAc)_2 \cdot H_2O$ in chloroform/methanol 1 : 1.3 produced green crystals suitable for single-crystal X-ray diffraction (SC-XRD) upon cooling the solution to room temperature. The positive-ion high-resolution ESI mass spectrum of the complex showed a peak with m/z 990.4615, which could be assigned to $[CuL^7 + H^+]^+$ and a peak with m/z 495.7338 attributed to the doubly charged ion $[CuL^7 + 2H^+]^{2+}$ (Fig. S14 and S15†). Both experimental isotopic patterns were in good agreement with theoretical isotopic distributions. The formation of the complex and its coordination geometry, as well as other peculiarities of the molecular structure of $[CuL^7]$ were established by SC-XRD.

X-ray crystallography

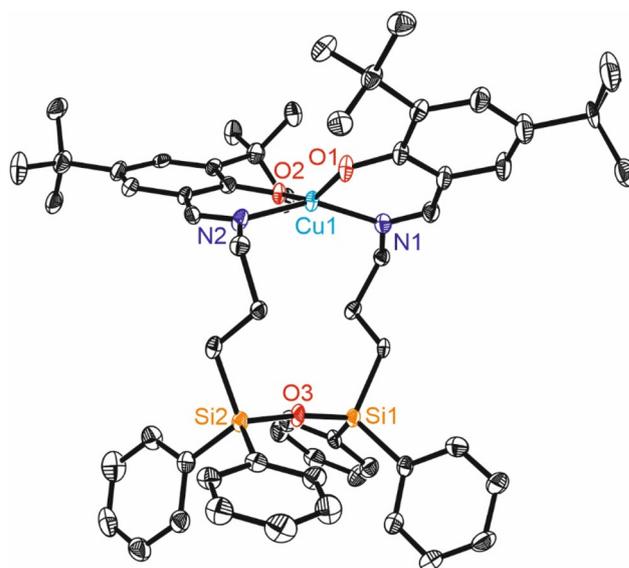The result of the crystallographic study of $[CuL^7] \cdot 0.875CHCl_3 \cdot 0.375CH_3OH$ is shown in Fig. 1. The

Fig. 1 ORTEP view of one of the two crystallographically independent molecules of $[CuL^7]$ with heteroatom labeling and thermal ellipsoids at the 50% probability level. The H atoms are not shown for clarity.

complex crystallized in a noncentrosymmetric monoclinic space group $P2_1$. There are two crystallographically independent molecules in the asymmetric unit. The crystal contains interstitial solvent ($CHCl_3$ and MeOH). In the following discussion, the co-crystallised solvent will not be included in the formula. Selected metric parameters, quite similar for both crystallographically independent molecules, are summarized in Table 1 and compared to those in related complexes $[CuL^1]$ and $[CuL^6]$ (see Chart 1, structure **III**). The tetradentate Schiff base is coordinated to Cu(II) *via* two phenolato oxygen donors O1 and O2 and two azomethine nitrogen atoms N1 and N2 (for the one crystallographically independent molecule of $[CuL^7]$ shown in Fig. 1). Upon coordination of the tetradentate ligand to Cu(II), two six-membered rings and one central 12-membered ring were formed as reported previously for other 3d metal complexes with analogous type **III** Schiff bases bearing a tetramethyldisiloxane unit (Chart 1, structure **III**).[2,3] The bond lengths from Cu(II) to N and O donor atoms are well-comparable with those in $[CuL^6]$ (Table 1). The Cu(II) ion has a strongly tetrahedrally distorted square-planar (N_2O_2) coordination geometry. The degree of tetrahedral distortion of coordination geometry in four-coordinate complexes characterised by three descriptors (τ_4,[15] τ_δ[16] and τ'_4[17]) yields values very close to 0.4 when applied to $[CuL^7]$ and comparable with those observed previously in $[CuL^1]$ and $[CuL^6]$ (see Table 1). The value of τ_4 in four-coordinate metal complexes varies from 0 for an ideal square-planar geometry to 1 for a perfect tetrahedral geometry. The values of τ_4, τ_δ and τ'_4 close to 0.4 are indicative of a see-saw or sawhorse coordination geometry in all these complexes.[18]

The Si–O–Si bond angle in $[CuL^7]$ with a tetraphenyldisiloxane unit is close to linear and larger by 11.5–12.5° than in the analogous complex $[CuL^6]$ with a tetramethyldisiloxane moiety

Table 1 Selected metric parameters for [CuL^7] and related complexes [CuL^1][3] and [CuL^6][6]

Bond length, Å	[CuL^7]^e	[CuL^1]	[CuL^6]
Cu1–N1 [Cu2–N3]^d	1.958(4) [1.953(4)]	1.960(2)	1.963(3)
Cu1–N2 [Cu2–N4]^d	1.962(5) [1.974(5)]	1.963(2)	1.965(3)
Cu1–O1 [Cu2–O4]^d	1.903(4) [1.897(4)]	1.882(1)	1.913(2)
Cu1–O2 [Cu2–O5]^d	1.892(4) [1.899(4)]	1.886(1)	1.899(2)
Si1–O3 [Si3–O6]^d	1.623(4) [1.629(4)]	1.629(4)	1.610(4)
Si2–O3 [Si4–O6]^d	1.626(4) [1.618(4)]	1.614(2)	1.616(3)
Bond angles (°)			
O1–Cu1–O2 [O4–Cu2–O5]^d	150.86(18) [153.27(17)]	147.77(7)	154.2(1)
O1–Cu1–N1 [O4–Cu2–N3]^d	93.7(2) [92.52(18)]	94.52(7)	92.7(1)
O2–Cu1–N1 [O5–Cu2–N3]^d	93.46(19) [93.50(19)]	95.65(7)	92.5(1)
O1–Cu1–N2 [O4–Cu2–N4]^d	93.33(18) [92.84(18)]	93.48(6)	94.3(1)
O2–Cu1–N2 [O5–Cu2–N4]^d	94.50(18) [93.41(18)]	94.26(7)	92.5(1)
N1–Cu1–N2 [N3–Cu2–N4]^d	149.9(2) [153.22(19)]	147.28(7)	153.1(2)
Si1–O3–Si2 [Si3–O6–Si4]^d	172.1(3) [173.8(3)]	169.75(2)	161.1(3)
τ_4^{a}	0.420 [0.380]	0.460	0.374
τ_δ^{b}	0.417 [0.380]	0.458	0.371
τ'_4^{c}	0.417 [0.379]	0.459	0.370

^{a} $\tau_4 = 360 - (\alpha + \beta)/141$, where α and β are the two largest angles at the Cu atom. ^{b} $\tau_\delta = \tau_4 \times (\alpha/\beta)$, where α and β are the two largest angles at the Cu atom. ^{c} $\tau'_4 = (\beta - \alpha)/(360 - \theta) + (180 - \beta/180 - \theta)$, where α and $\beta(\beta > \alpha)$ are the two largest angles at the Cu atom and the θ value is $\cos^{-1}(-1/3) \approx 109.5°$. ^{d} Second crystallographically independent molecule in the asymmetric unit. ^{e} The actual formula is [CuL^7]·0.875CHCl$_3$·0.375CH$_3$OH.

(see Table 1). This is likely due to stronger repulsions between phenyl groups in [CuL^7] than between the methyl groups attached to Si atoms in [CuL^6], while the tetrahedral distortion of the square-planar coordination geometry is substantial and close in both complexes (see Table 1). Wide variability of the Si–O–Si bond angle is reported in the literature. Specifically, in dioxadisilethane, it is 93.5°,[19] and in quartz, it is 143.7°,[20] while in hexaphenyldisiloxane, this angle is linear.[21,22] In contrast to the linear Si–O–Si angle in Ph$_3$Si–O–SiPh$_3$, the C–O–C angles in Ph$_3$C–O–CPh$_3$ and Ph$_2$CH–O–CHPh$_2$ are 127.8 and 113.3°, respectively.[23–25] The close to linear Si–O–Si angle is not only the result of minimisation of the effects of steric repulsion of the phenyl groups and optimisation of the delocalisation of the electron density between the oxygen and silicon atoms, but also due to the predominantly ionic character of the Si–O bonds and the highly polarised covalent Si–C bonds.[2] This was evidenced by both charge density and DFT calculations, which disclosed that the second derivative of electron density at the bond critical points (BCPs) $\nabla^2\rho$ (r_{BCP}) for the two Si–O bonds in [CuL^1] is positive, as was also the case for difluorobis[N-(dimethylamino)phenylacetimidato-N,O]silicon[26] with a predominantly ionic character of the Si–O bond and NaCl.[2]

The crystal structure consists of neutral molecules [CuL^7] which form channels along the a-axis of the unit cell, in which interstitial chloroform and methanol molecules are localised. The volume of the voids per unit cell is 666.9 Å^3 (see Fig. S16 in the ESI†).

Cyclic voltammetry and spectroelectrochemistry

The cyclic voltammogram (CV) of [CuL^7] in dichloromethane (DCM) in the presence of 0.1 M tetrabutylammonium hexafluorophosphate (nBu$_4$NPF$_6$) as a supporting electrolyte shows two reversible oxidations in the anodic region at 0.55 and 0.85 V $vs.$ the ferricenium/ferrocene couple as shown in Fig. 2a.

The optical spectrum of [CuL^7] in DCM shows three strong absorptions with maxima at 275, 327 and 380 nm and one weak and broad absorption between 550 and 750 nm (Fig. 2b, blue trace). The detailed characterisation of the observed transitions will be provided in the theoretical part below. The broad-line EPR spectrum of [CuL^7] in 0.2 M nBu$_4$NPF$_6$ in DCM at room temperature (inset in Fig. 2b) is characteristic of paramagnetic Cu(II) (d^9, $S_{Cu} = \frac{1}{2}$).

Upon anodic oxidation of [CuL^7] in 0.2 M nBu$_4$NPF$_6$ in DCM at the first oxidation peak, the optical bands at 275, 327 and 380 nm decrease and a new UV band at 304 nm emerges (Fig. 3a). Simultaneously, several weak optical bands appear in the vis–NIR region at 530, 880 and 1500 nm (Fig. 3b), which are typical of phenoxyl radicals (difference spectra were measured during the experiment due to the low-intensity transitions in the vis–NIR region).[27] A decrease in the intensity of the room-temperature Cu(II) (d^9, $S_{Cu} = \frac{1}{2}$) EPR signal was also observed after anodic oxidation of [CuL^7] in 0.2 M nBu$_4$NPF$_6$ in DCM when using a large Pt mesh working electrode (Fig. 3c). Additionally, a new EPR spectrum characteristic of an organic radical (g factor ~2.002) appears at more positive potentials (see the details in Fig. 3d).

Upon progressing to the region of the second oxidation peak, the optical band at 304 nm steadily increases, as shown in Fig. 4a. All oxidation processes seem to be chemically reversible as illustrated by the 3D plots of the spectroelectrochemical responses in Fig. 4c and d.

We also studied the optical absorption properties of the chemically oxidised complex [CuL^7] using tris(4-bromophenyl)ammoniumyl hexachloroantimonate (Magic Blue, **MB**) as a single-electron oxidising agent. The vis–NIR absorption spectra resulting from the chemical oxidation of the initial [CuL^7] (black trace) in DCM using **MB** (red trace: 0.8 equiv.; blue trace: 1.1 equiv.) are shown in Fig. 5a. The corresponding
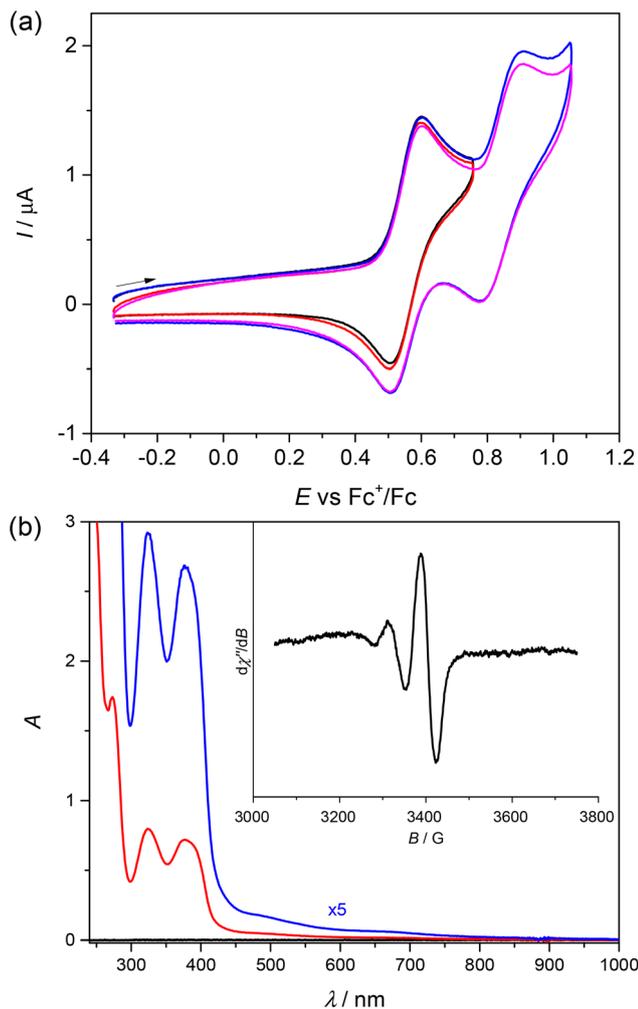
Fig. 2 (a) Cyclic voltammograms (two consecutive scans) of 0.5 mM [CuL^7] in DCM/0.1 M nBu$_4$NPF$_6$ on a GC disc working electrode, scan rate 100 mV s^{-1}; (b) optical and EPR (inset, 0.5 mM [CuL^7]) spectra of [CuL^7] in DCM/0.2 M nBu$_4$NPF$_6$ at room temperature (red trace: 45 μM [CuL^7], the blue trace shows an expansion (5×) in the vis–NIR region, optical path length 10 mm).

spectrum measured after one-electron anodic oxidation of [CuL^7] in DCM/0.2 M nBu$_4$NPF$_6$ (Fig. 5b) is well-defined and almost identical to those recorded upon chemical oxidation (Fig. 5a).

Considering a quite recent comprehensive review describing the properties and reactivities of a variety of Cu(II)-phenolato and Cu(II)-phenoxyl radical complexes,[28] we compared the experimentally measured vis–NIR spectra of the mono-oxidised species [CuL^7]$^+$ with the well-documented examples of one-electron oxidised Schiff base complexes with substituted phenolato moieties.[29–32] These Cu(II)-salen-type complexes were oxidised to form mainly the Cu(II)-phenoxyl radical species with the localised unpaired electron on one of the two phenolic moieties both in the solid state and in solution. Note that our vis–NIR spectra are very similar to those reported for Cu(II)-phenoxyl radical species. The X-ray diffraction structures clearly suggested that the unpaired electron is mainly localised

on one of the two phenolic moieties.[29–31] Therefore, based on these literature data and on the Robin and Day classification of mixed-valence systems, the NIR band at 6490 cm^{-1} (1540 nm) can be well described as the intervalence charge transfer (IVCT) band of Class II with a Cu(II)-localised phenoxyl radical.

Thus, [CuL^7] can be reversibly oxidised by two successive one-electron processes with the generation of stable phenoxyl mono- and diradicals as also reported previously for other systems.[27,33] In other words, both oxidations are ligand-centred and lead to the formation of coordinated phenoxyl radicals [CuL^7]$^{•+}$ and [CuL^7]$^{2•2+}$. Copper(II)-phenoxyl mono-radical species are known to undergo intramolecular magnetic exchange interactions between the unpaired electron on the Cu(II) d-orbital (d^9, $S = \frac{1}{2}$) and the phenoxyl radical ($S_{rad} = \frac{1}{2}$) leading to either the diamagnetic ground state ($S_T = 0$) via antiferromagnetic spin coupling or the triplet $S_T = 1$ ground state via ferromagnetic spin–spin interaction. In both cases, full or nearly full disappearance of the EPR signal is observed. The nearly silent triplet ground state is difficult to observe because of its closeness to the X-band energy quantum (0.35 cm^{-1}) zero-field splitting parameters documented for Cu(II) phenoxyl radical salen-type complexes.[34–36] This intramolecular magnetic spin interaction will be discussed in more detail below.

Theoretical calculations

Geometry optimisation. The structure of [CuL^7] was optimised in various solvents as well as in a vacuum. The calculated geometries of [CuL^7] are close with only slight variations in the dihedral angle θ(O–N–O–N). These variations depend on the optimisation criteria, showing some degree of flexibility in every case. Thus, the real absorbance spectra represent a superposition of the set of geometries, eventually leading to line broadening. The final optimisations were done at the PBE0/def2-TZVP/D4 level in all cases. The solvation effects were considered through the implicit SMD model. The variations of the dihedral angle θ(O–N–O–N) depending on the conditions are summarized in Table 2. As can be seen, the variations are only minor and are within the geometry optimisation convergence criteria.

Optical spectrum and magnetic interactions. The large size of the whole molecule of [CuL^7] (142 atoms) imposed the isolation of the copper(II) chromophore from the disiloxane backbone to reduce the computational costs of excited-state calculations. The truncation of the alkane chains with the disiloxane unit and saturation of the remaining positions with H-atoms resulted in the molecule [CuL^{7}c] with 97 atoms. Although the siloxane part is not presumed to participate in the redox processes and low-energy excitation, the TDDFT calculations at the light level (PBE0/ma-def2-SVP) were performed for [CuL^7] and [CuL^{7}c] to ensure the coincidence of the predicted absorption spectra in the middle and low energy regions. As can be seen in Fig. 6a, the spectra show almost no difference at $\lambda > 260$ nm. The predicted band at 254 nm is only slightly affected in terms of its intensity, and the higher-energy spectrum shows significant differences due to the excitation
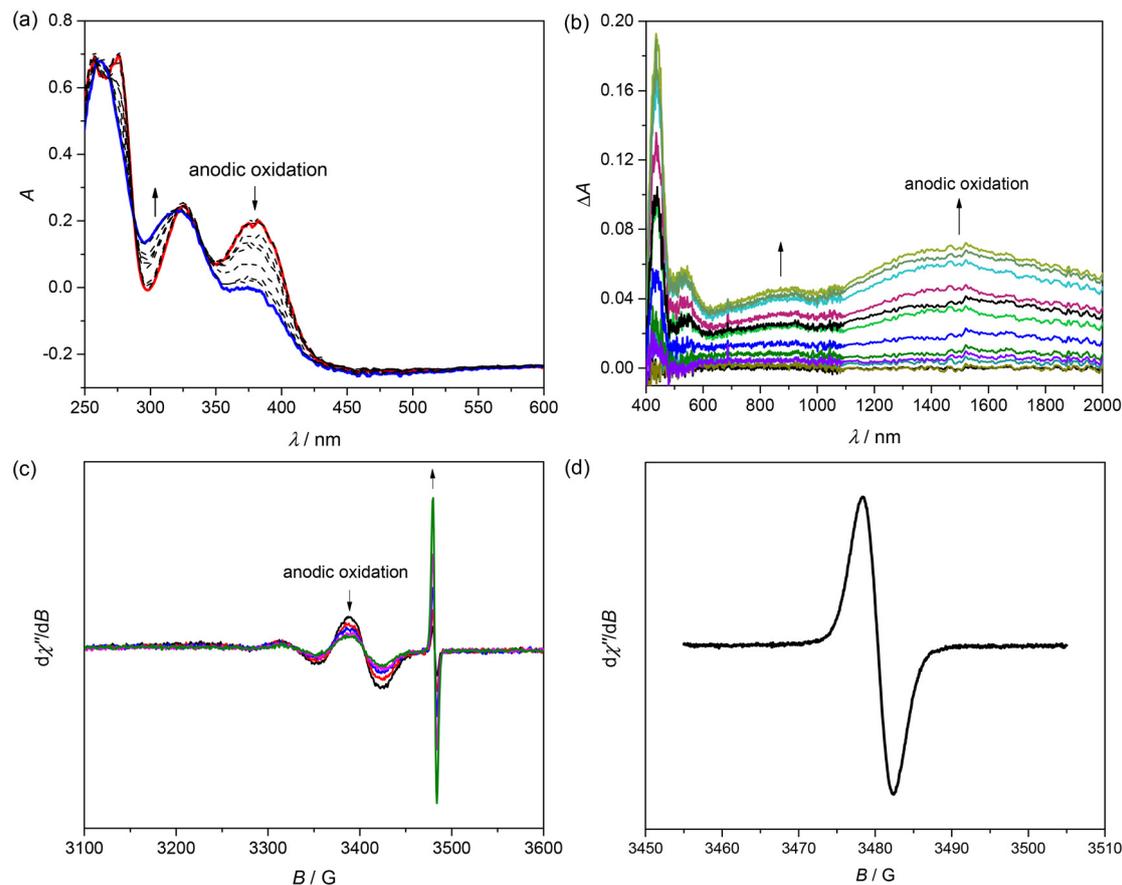
Fig. 3 (a) UV−vis spectra and (b) difference vis−NIR spectra measured during spectroelectrochemistry of 75 µM [**CuL**^{7}] in 0.2 M nBu$_4$NPF$_6$ in DCM in the region of the first anodic peak (Pt honeycomb working electrode, optical path length 1.7 mm, scan rate 10 mV s^{-1}); (c) changes in EPR spectra measured upon spectroelectrochemistry of 0.5 mM [**CuL**^{7}] in the region of the first anodic peak (Pt mesh working electrode, potentiostatic oxidation, room temperature); and (d) details of the EPR spectrum observed upon oxidation characteristic of organic radicals (sweep width 50 G; centre field 3480 G; modulation amplitude 1 G).

within the siloxane fragment not accounted for by [**CuL**^{7}**c**]. Therefore, for the region $\lambda > 260$ nm, the proposed [**CuL**^{7}] → [**CuL**^{7}**c**] truncation was considered as producing accurate results. Here and further, all calculations are reported for DCM solvation medium, except for the multiconfigurational random-phase approximation (MC-RPA) ones.

The compound [**CuL**^{7}**c**] was subjected to TDDFT calculations at the PBE0/aug-cc-pVDZ-DK/aug-cc-pVTZ-DK (for Cu) level. The presence of diffuse functions in the basis set is known to be essential for accurate prediction of the energies of excited states.[37] The numerical results of the TDDFT calculations strongly depend on the DFT functional; thus a careful choice of the latter is crucial for obtaining relevant spectra. The PBE0 functional was earlier demonstrated to have a balanced accuracy for TDDFT calculations of metal complexes, and hence, it was used in the present case.[38,39] The theoretical UV−vis spectrum in the range of 200–1000 nm is shown in Fig. 6b.

The four lowest-energy excited states S_1–S_4 originate from d–d transitions, while the others are mostly due to the aromatic fragments of the ligands. The overall view of the TDDFT spectrum follows the experimental one. The most prominent bands of the spectrum are due to the strong transitions to the S_{12}, S_{21} and S_{31} excited states (340.3, 300.5 and 254.2 nm, respectively). While the S_{12} and S_{31} states are of the typical $\pi \to \pi^*$ nature and originate from the transitions within the aromatic fragments of the ligands, the S_{21} state has the LMCT $\sigma \to$ d character involving the $d_{x^2-y^2}$ orbital of Cu(II).

Despite the efficiency of the TDDFT method for the prediction of the $\pi \to \pi^*$ transitions, it lacks accuracy in the description of the lower-energy transitions within the d-shell of the metal centres. The presence of a single metal ion in [**CuL**^{7}**c**] enabled the possibility of Ab Initio Ligand Field Theory (AILFT) calculations based on the CAS(9,5) active space with the NEVPT2 correction. Here and further, the CASSCF studies were performed employing the def2-TZVP basis set for Cu(II), its N,O-donor coordination environment and the carbon atoms of the aromatic rings and Schiff base groups, keeping all other atoms at the def2-SVP level. The fully occupied orbitals of Cu(II) in the [**CuL**^{7}**c**] group in two degenerate levels d_{xz}/d_{xy} and d_{z^2}/d_{yz}, while the singly occupied $d_{x^2-y^2}$ one has significantly higher energy (Fig. 6c). The CAS(9,5) space allows for
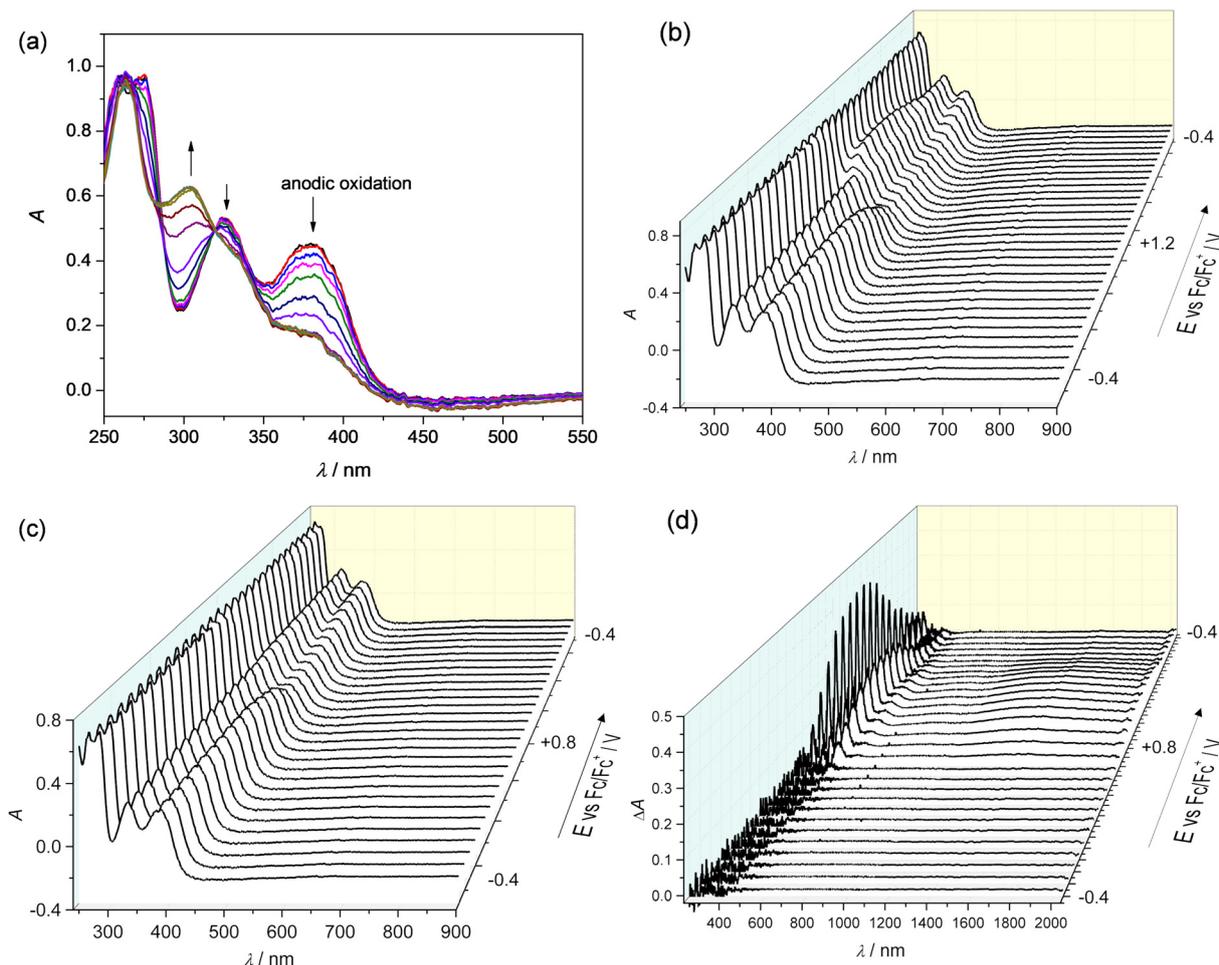
Fig. 4 (a) UV−vis spectra measured upon spectroelectrochemistry of 150 μM [**CuL⁷**] approaching the region of the second anodic peak. Evolution of UV−vis−NIR spectra in a 3D graph measured upon spectroelectrochemistry of 75 μM [**CuL⁷**] in 0.2 M nBu₄NPF₆ in DCM approaching the region of the (b) second and (c) first anodic peaks; (d) difference vis−NIR spectra measured during CV in the region of the first anodic peak (Pt honeycomb working electrode, optical path length 1.7 mm, scan rate 10 mV s⁻¹).

four possible transitions to the S_1–S_4 states, from which the excitation $S_0 \rightarrow S_4$ ($d_{z^2} \rightarrow d_{x^2-y^2}$) is the strongest one. The broad line has a maximum at 547.0 nm (Fig. 6d) which matches well with the experimentally observed shoulder at 600 nm (see Fig. 2b).

The interaction of the five d-orbitals and all p_z orbitals of the aromatic rings results in the huge CAS(21,17) active space which, unfortunately, under our conditions could not be handled in a reasonable time even with ICE or DMRG approximations. Another obstacle is the limited participation of the lower-lying Cu(II) d-orbitals in the excited states, which results in their occupations close to 2 with the subsequent tendency of these orbitals to run out from the active space. Therefore, for further studies, we have limited the active space by involving only one Cu(II) d-orbital (the half-occupied $d_{x^2-y^2}$ one) leading to a reasonable CAS(13,13) state-averaged calculation with 6 roots. The respective active space natural orbitals are depicted in Fig. S17.† They can be grouped into π-bonding and π-antibonding orbitals as well as the Cu(II) $d_{x^2-y^2}$ orbital. As for

AILFT calculations, the ground state of [**CuL⁷c**] in terms of the CAS(13,13) space features an unpaired electron located on the $d_{x^2-y^2}$ orbital, while the π-bonding ones are doubly occupied.

The absorption spectrum reconstructed from the CAS (13,13) study of [**CuL⁷c**] is shown in Fig. S18,† right. Only the $S_0 \rightarrow S_5$ transition shows a notable oscillator strength with a wavelength of 288.1 nm. This transition is of the π → π* type and involves several excitations, from which one is dominant (57%). The corresponding excitation S_{31} from the TDDFT calculation has a close wavelength of 254.2 nm (Fig. 6b). The excited states of [**CuL⁷c**] were also evaluated using the MC-RPA model with the CAS(1,2) state-specific starting configuration and 14 roots. Although the overall shape of the MC-RPA-generated spectrum (Fig. S19†) does not fit well with the experimental one, it correctly predicts the grouping of the transitions into the weak d → d and strong π → π* ones. The singly oxidised forms of [**CuL⁷**] were optimised and truncated in the same manner as the non-oxidised form produces ³[**CuL⁷c**]⁺, ²[**CuL⁷c**]²⁺ and ⁴[**CuL⁷c**]²⁺ model fragments. The vertical and
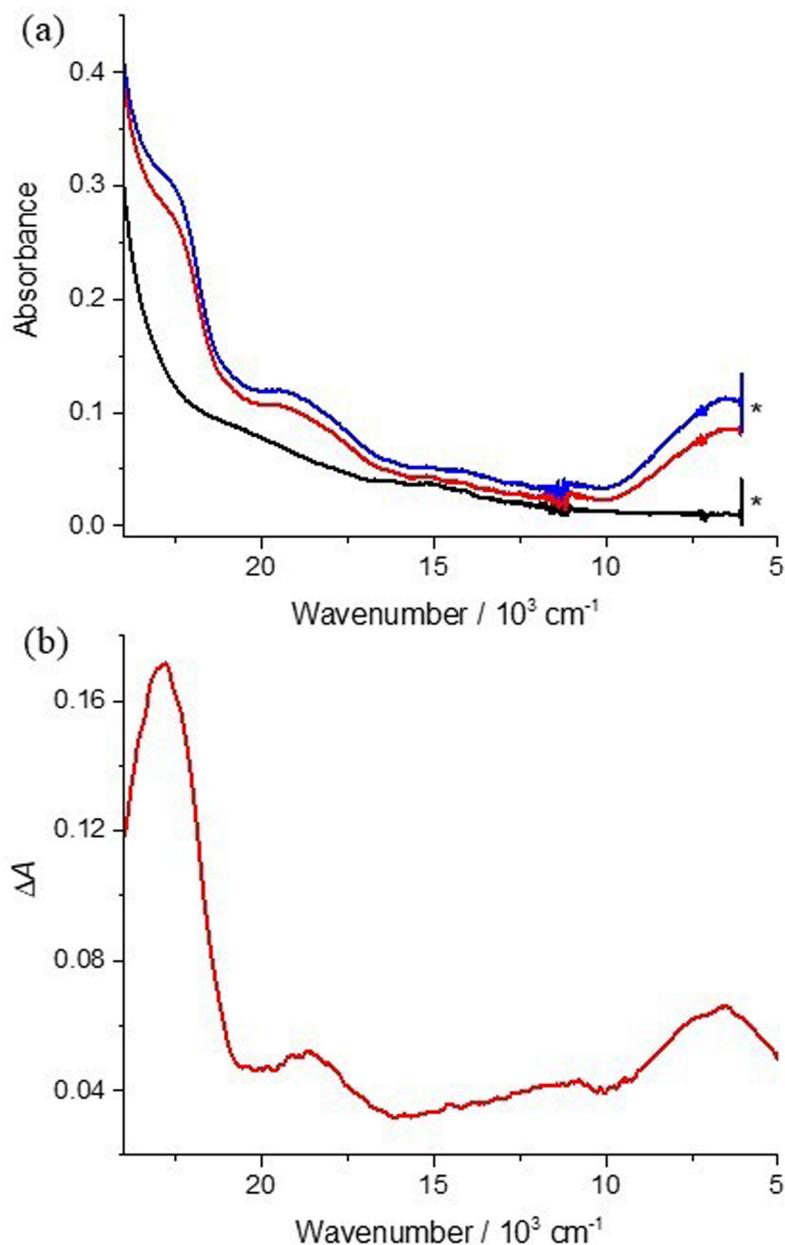
Fig. 5 (a) Vis–NIR absorption spectra measured after the chemical oxidation of [**CuL⁷**]⁰ (black trace) in DCM with **MB** as an oxidising agent (red trace: 0.8 equiv., blue trace: 1.1 equiv.). The stars indicate spectral 'holes' due to solvent absorption; (b) experimental vis–NIR spectrum of anodically oxidised [**CuL⁷**]⁰ in DCM/0.2 M nBu$_4$NPF$_6$ in the region of the first anodic peak.

Table 2 Dihedral angle θ(O–N–O–N) depending on the optimisation conditions

	No solv.	CH$_2$Cl$_2$	CyH	MeCyH	*cis*-1,2-DMCH	MeCN	MeOH
Angle	−21.39	−23.97	−23.24	−23.23	−23.19	−23.79	−24.24

adiabatic first ionisation energies of [**CuL⁷**] were estimated to be 5.4 and 5.2 eV, respectively (PBE0/def2-TZVPP single-point energies after PBE0/def2-TZVP optimisation in DCM medium). The small difference in these values originates from the close geometries of the natural ([**CuL⁷**]) and oxidised (³[**CuL⁷**]⁺) forms. The dihedral θ(O–N–O–N) for ³[**CuL⁷**]⁺ is −25.56°. Remarkably, an attempt to optimise the oxidised form in a singlet state failed, producing an unrealistic geometry with "twisted" ligands. The spin densities obtained at the various levels of theory are shown in Fig. 7a.
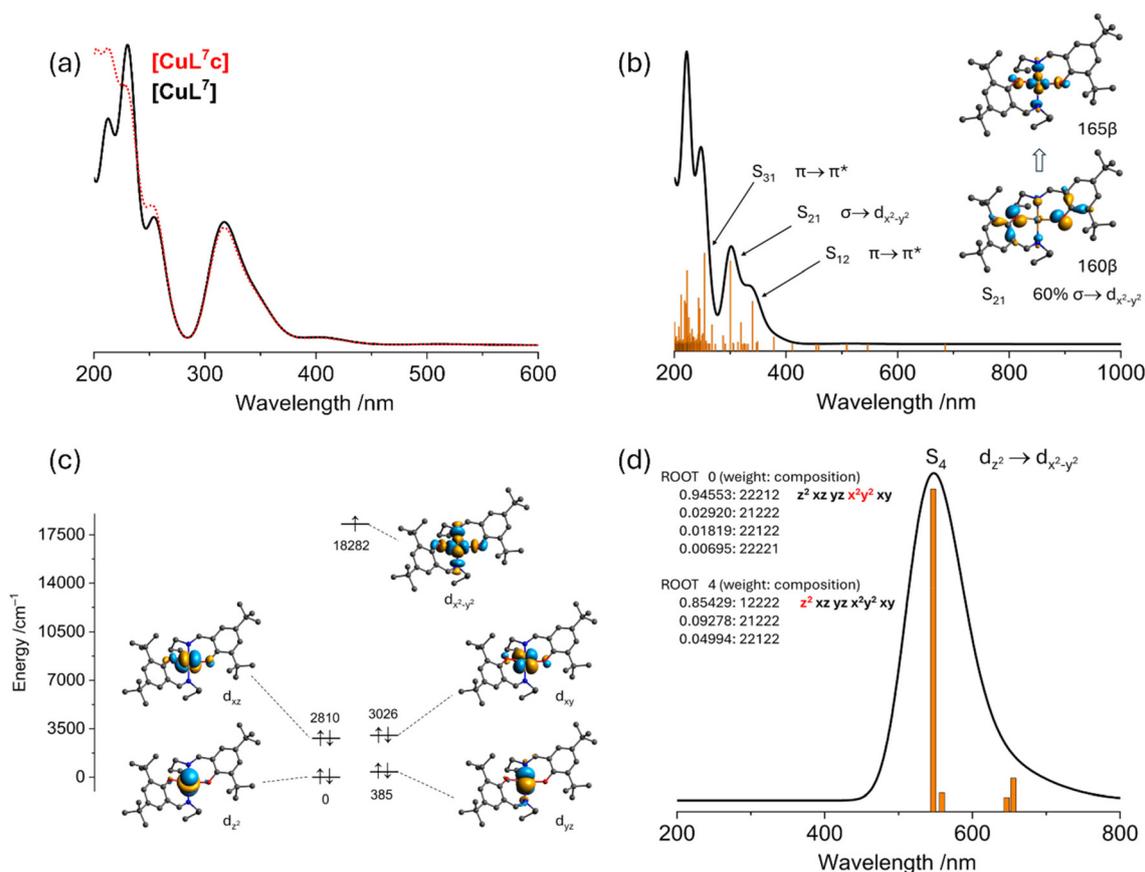
Fig. 6 (a) TDDFT theoretical UV–vis spectra of **[CuL⁷]** (black trace) and **[CuL⁷c]** (red trace) calculated at the PBE0/ma-def2-SVP (all atoms) level involving the SMD (DCM) model; (b) TDDFT theoretical UV–vis spectra of **[CuL⁷c]** calculated at the PBE0/aug-cc-pVDZ-DK/aug-cc-pVTZ-DK (for Cu) level involving the SMD (DCM) model. The isosurfaces of the natural transition orbitals corresponding to the $S_0 \rightarrow S_{21}$ transition are shown; (c) the relative energies and isosurfaces of the five d-orbitals of a copper centre calculated at the AILFT CAS(9,5)/SC-NEVPT2 level using def2-SVP/def2-TZVP basis sets. The occupations correspond to the ground state configuration with a weight of 94.6%; (d) theoretical UV–vis absorption spectrum constructed from the d $\rightarrow$ d excitation calculated at the AILFT level. Compositions of the S_0 and S_4 excited states corresponding to the strongest transition are indicated on the left (singly occupied atomic orbitals are highlighted in red).

Both DFT and state-specific CASSCF predict the unpaired electrons to be localised on the $d_{x^2-y^2}$ copper(II) orbital and the ligand-centred molecular orbital that involves p_z carbon and oxygen atomic orbitals. The DFT broken-symmetry calculation of ^{3}**[CuL⁷c]**$^+$ predicts the ferromagnetic ground state with $J = 252.08$ cm^{-1} (for $\hat{H} = -2J\hat{S}_1\hat{S}_2$ Hamiltonian), confirming the triplet spin state to be energetically favorable. The calculations performed for the whole ^{3}**[CuL⁷]**$^+$ molecule resulted in a very close value of $J = 251.83$ cm^{-1}. These observations indicate that the influence of the siloxane moiety on the electronic structure of the Cu(II) chromophore is negligible, in agreement with the above TDDFT studies (Fig. 6a). The unrestricted corresponding ("magnetic") orbital of the broken-symmetry solution shows an overlap value $S = 0.0023$, where the α and β operators indicate the interacting electrons to be localised in the same manner as for SS-CASSCF and DFT (Fig. 7b). The inability to see the $S = 1$ EPR signal after the one-electron oxidation step in our experiments even at low temperatures might be due to the properties of the triplet being unsuitable for

observation by conventional X-band EPR spectroscopy and by the temperature limit (100 K) in our laboratory.

The state-averaged CAS(12,13) solution resulted in the triplet ground spin state after the SC-NEVPT2 correction, with the first singlet state lying 112 cm^{-1} above. The absorption spectrum reconstructed from the CAS(12,13)/NEVPT2 calculated excitation energies and oscillator strengths is shown in Fig. 7c, left. The three lowest excitations are of $\pi \rightarrow \pi^*$ nature, where the acceptor π-bonding orbital is singly occupied, stipulating the low energy of these transitions. No transitions involving the Cu(II) $d_{x^2-y^2}$ orbital were observed. The excited states S_4 and S_5 of low intensity are based on the $\pi \rightarrow \pi^*$ transitions.

The TDDFT calculations of ^{3}**[CuL⁷c]**$^+$ confirm the presence of a strong absorption band in the vis–NIR region (Fig. 8a). As for CASSCF studies, the first excited state involves the singly occupied π-orbital as an acceptor. The following series of transitions to the S_2–S_5 states is in the low-energy visible region and comprises $\pi \rightarrow \pi^*$ and $\pi \rightarrow$ d transitions. The structure of the UV region is only slightly affected by the oxidation of the
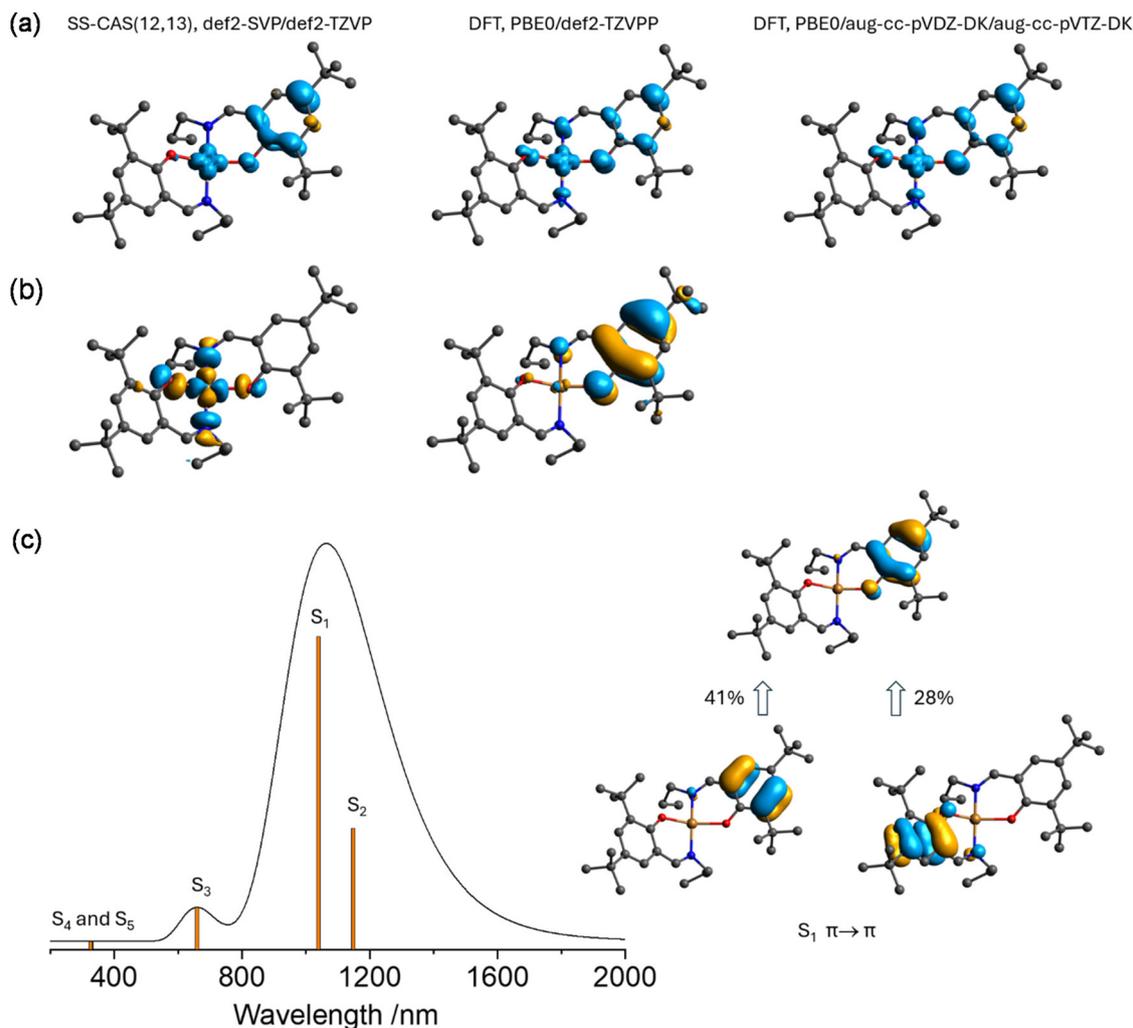
Fig. 7 (a) Isosurfaces of spin densities of $^3[\mathbf{CuL^7c}]^+$ calculated at the stated levels of theory; (b) isosurfaces of the spin-up and spin-down unrestricted corresponding orbitals of the broken symmetry solution of $^3[\mathbf{CuL^7c}]^+$ calculated at the PBE0/def2-TZVPP level; (c) left: theoretical visible absorption spectrum and transitions of $^3[\mathbf{CuL^7c}]^+$ calculated at the SA-CAS(12,13)/NEVPT2 level; right: isosurfaces of natural active space orbitals responsible for the strongest excitation ($S_0 \rightarrow S_1$).

molecule. The MC-RPA model applied for $^3[\mathbf{CuL^7c}]^+$ starting from the CAS(2,2) state-specific solution also showed an increase in low-energy absorbance, showing the transitions of similar nature (Fig. 8b).

From the DFT single-point and broken-symmetry calculations, as well as the CASSCF ones, all indicating the triplet ground spin state, the existence of $^3[\mathbf{CuL^7c}]^+$ with a formal Cu (I) or Cu(III) oxidation state is not likely. To further correlate these results with the experimental data, we calculated the adiabatic ionisation energies of a series of related copper(II) complexes with salen-type ligands, for which the redox potentials have been determined under similar conditions.[28] After optimisation of the respective non-oxidised doublet and oxidised triplet forms and calculation of the single-point energies at the higher DFT level (ωB97M-V/def2-QZVPP), a clear dependence of the redox potential *vs.* ionisation energy appeared (Fig. S20, Tables S2 and S3†). Within this dependence, the

position of the complex $[\mathbf{CuL^7}]$ stands far from that of compound **f** (Fig. S20†) for which the formal Cu(III) oxidation state was proposed upon (electro)chemical oxidation in solution,[40] providing further evidence of the Cu(II) oxidation state in the one-electron oxidised $[\mathbf{CuL^7}]$.

DFT geometry optimisations of the doubly oxidised complex $[\mathbf{CuL^7}]$ were performed for both doublet and quartet spin states, $^2[\mathbf{CuL^7c}]^{2+}$ and $^4[^4\mathbf{CuL^7c}]^{2+}$, resulting in indistinguishable geometries (Fig. 9a). Hence, both these structures can be used for calculations of both ground spin states. The DFT single-point calculations at the ωB97M-V/def2-QZVPP level indicated $\Delta E = 401.9$ cm^{-1} between $^4[\mathbf{CuL^7c}]^{2+}$ and $^2[\mathbf{CuL^7c}]^{2+}$ with the prevalence of the quartet state. The TDDFT predicts that the spectra of $^2[\mathbf{CuL^7c}]^{2+}$ and $^4[\mathbf{CuL^7c}]^{2+}$ are almost equal with the lowest transition located around 800 nm (Fig. 9b). The DFT-calculated spin densities of the quartet state show an expected plot with the three unpaired electrons dis-
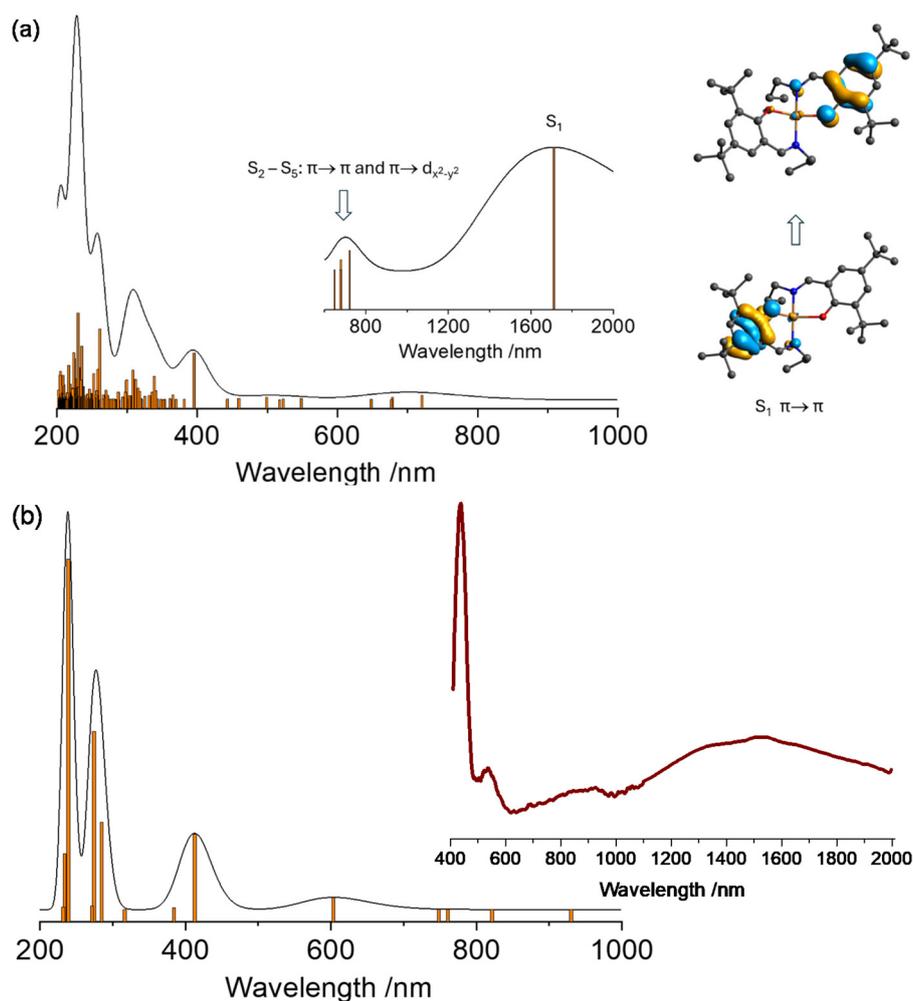
Fig. 8 (a) TDDFT theoretical UV–vis spectra of $^3[\mathbf{CuL^7c}]^+$ calculated at the PBE0/aug-cc-pVDZ-DK/aug-cc-pVTZ-DK (for Cu) level involving the SMD (DCM) model. The isosurfaces of the natural transition orbitals corresponding to the $S_0 \rightarrow S_1$ transition are shown on the right. (b) UV–vis spectrum and transitions calculated at the MC-RPA level for $^3[\mathbf{CuL^7c}]^+$. Representative experimental vis-NIR spectrum of anodically oxidised $[\mathbf{CuL^7}]$ in DCM/0.2 M nBu$_4$NPF$_6$ in the region of the first anodic peak is shown on the right.

tributed over the π ligand and Cu(II) d$_{x^2-y^2}$ orbitals (Fig. 9b, right), while in the doublet model, the single unpaired electron is located on the broad molecular orbital that involves both aromatic ligands (Fig. 9b, left). Hence, the CASSCF studies were invoked to understand the physical nature of these states.

The SA-CAS(11,13) calculations with the SC-NEVPT2 ones on top of that suggested the quartet ground spin state of doubly oxidised $[\mathbf{CuL^7c}]^{2+}$. However, in contrast to the $[\mathbf{CuL^7c}]^+$ species, the first state of different multiplicity is practically of the same energy as the ground state $\Delta E = 11.7$ cm^{-1} and the next doublet state is 145.4 cm^{-1} above the ground quartet state. The electron configuration of the lowest doublet state is of multideterminant character where the two π-bonding orbitals of the ligand have almost equal [20] and [02] configurations, while the Cu(II) d$_{x^2-y^2}$ orbital remains singly occupied. The $^4S_0 \rightarrow {}^4S_1$ excitation is located at 780 nm and constitutes π → π* transitions (Fig. S21†). No excitations in the NIR region

were found. The MC-RPA calculations based on the SS-CAS (3,3) ground state also confirm the absence of NIR-located transitions (Fig. S22†).

Catalysis. The solubility of $[\mathbf{CuL^7}]$ in apolar solvents inspired us to test the catalytic activity of this complex in the solvent-free oxidation of hydrocarbons using cyclohexane as a model substrate (Scheme 2). It should be stressed that the copper(II) complexes are known to be highly active in this kind of reaction, which, however, commonly proceeds in polar media to ensure the solubility of the catalyst.[7,41] Before testing alkane-soluble peroxides, a biphasic test using H$_2$O$_2$ as the terminal oxidant was performed. The compound was dissolved in cyclohexane ($[\mathbf{CuL^7}]_0 = 1$ mM), layered with H$_2$O$_2$ (to reach a 1 M concentration, if completely mixed in cyclohexane) and stirred at 50 °C. Analysis of the reaction products after 24 h disclosed only traces of the expected products, cyclohexanol and cyclohexanone. However, an important observation was the detection of cyclohexyl hydroperoxide (Fig. S23†) from its character-
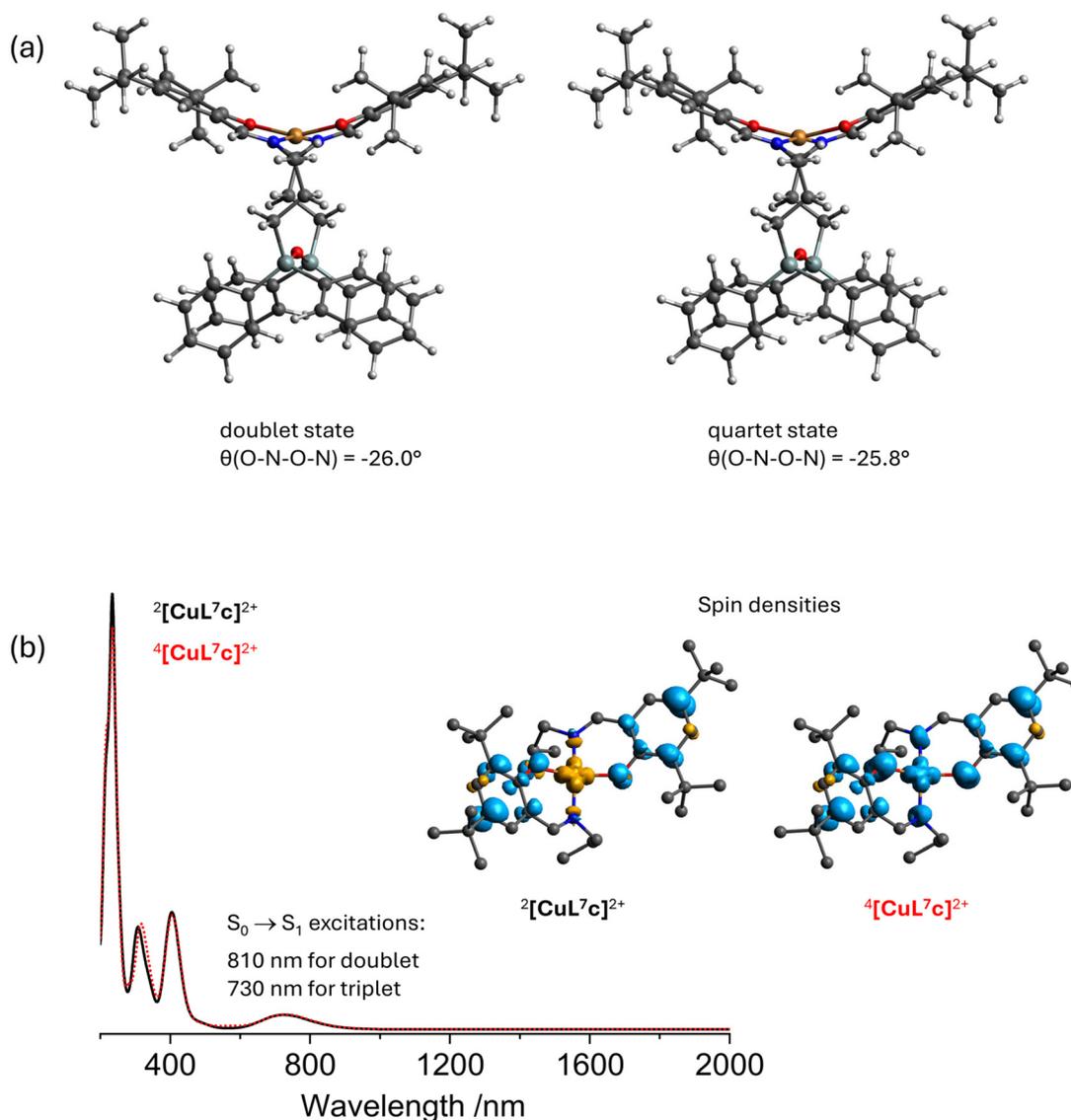
Fig. 9 (a) Molecular structures of ^{2}[CuL^{7}c]$^{2+}$ and ^{4}[CuL^{7}c]$^{2+}$ indicating the dihedral angle describing the distortion of the coordination polyhedron of a copper centre. DFT optimisation was performed at the PBE0/def2-TZVP/D4 level involving the SMD (CH$_2$Cl$_2$) solvation model. (b) TDDFT theoretical UV−vis spectra of ^{2}[CuL^{7}c]$^{2+}$ and ^{4}[CuL^{7}c]$^{2+}$ calculated at the PBE0/aug-cc-pVDZ-DK/aug-cc-pVTZ-DK (for Cu(II)) level involving the SMD (DCM) model. The isosurfaces of the spin densities for ^{2}[CuL^{7}c]$^{2+}$ and ^{4}[CuL^{7}c]$^{2+}$ calculated at the same level are shown on the right.
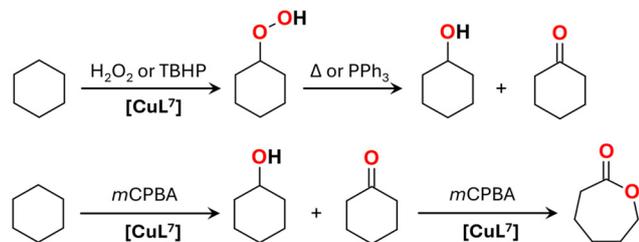
Scheme 2 Solvent-free oxidation of cyclohexane with H$_2$O$_2$, *tert*-butyl hydroperoxide (TBHP) and *m*-chloroperoxybenzoic acid (*m*CPBA) catalyzed by [CuL^7].

istic electron impact mass spectrum.[42–44] Alkyl hydroperoxides are expected products of free radical non-chain catalytic reactions, where the H$_2$O$_2$ molecule is transformed into a highly active hydroxyl radical.[41,42,45,46] Participation of a redox-active metal centre, such as Cu(II), is common in this kind of catalytic process, where copper shows Cu(I) and Cu(II) oxidation states. As the unstable cyclohexyl hydroperoxide (CyOOH) can be produced only from the non-chain oxidation of cyclohexane,[47] we can conclude that [CuL^7] acts as a catalyst. Treatment of the reaction mixture mainly containing CyOOH with PPh$_3$ quantitatively reduced the hydroperoxide to the respective alcohol (Fig. S24†).

Replacement of H$_2$O$_2$ as an oxidant with *tert*-butyl hydroperoxide (TBHP) under similar solvent-free conditions (1 M of

the oxidant) resulted in a large amount of CyOOH (Fig. S24 and S25†). The peak of CyOOH (Fig. S25†) underwent gradual disappearance upon the addition of PPh$_3$ due to its quantitative reduction to cyclohexanol, leading to a high alcohol/ketone ratio of 3.7 (Fig. S24†). The final total yield of cyclohexanol and cyclohexanone was 9.0% relative to TBHP. A notable amount of di-*tert*-butylperoxide, DTBP, was detected as a reaction product, indicating the participation of long-lived tBuO• radicals in the catalytic cycle (Fig. S26†).

Solvent-free oxidation of cyclohexane with *m*-chloroperoxybenzoic acid (*m*CPBA) was performed by using a lower concentration of the oxidant (0.1 M) due to the limited solubility of *m*CPBA in hydrocarbons and due to the production of a large amount of poorly soluble *m*-chlorobenzoic acid (*m*CBA). As *m*CPBA can produce a range of radical species (ArC(O)OO•, ArC(O)O• and Ar•) as well as oxidise substrates *via* a concerted mechanism (Scheme 3),[48,49] identification of the exact mechanism of *m*CPBA action is often a challenging task. The main products obtained after 24 h of the solvent-free reaction of *m*CPBA with cyclohexane catalysed by [**CuL**^{7}] (1 mM) are cyclohexanol, ε-caprolactone and cyclohexene oxide (Fig. S27†), while only traces of cyclohexanone were detected. The latter fact can be explained by the efficient Baeyer–Villiger reaction of cyclohexanone with *m*CPBA catalysed by [**CuL**^{7}] (Scheme 2). Hence, the formation of ε-caprolactone requires 2 equiv. of *m*CPBA, which should be taken into account when calculating the yields. The overall yield of products is 62.4% relative to *m*CPBA, of which 29.1% corresponds to cyclohexanol, 3.0% to cyclohexene oxide and 29.8% to ε-caprolactone. The yield of cyclohexanone does not exceed 0.5%. A blank test in the absence of the catalyst gave cyclohexanol as a single product with 3.0% yield after 24 h.

Oxidation of methylcyclohexane revealed a normalised 3°:2° selectivity of 15:1 which is consistent with the participation of ArC(O)O• as an H-abstracting radical.[50,51] The absence of stereoselectivity in the oxidation of *cis*-1,2-dimethylcyclohexane (ESI and Fig. S28–S31† there) agrees with the above assumption, confirming the existence of long-lived alkyl radicals in accordance with the homolytic O–O *m*CPBA bond splitting route (Scheme 3). However, the amount of chlorobenzene as a side product generated by the [**CuL**^{7}]/*m*CPBA catalytic system upon the oxidation of cyclohexane is surprisingly low,

only 2.5%. This result contradicts the common observation of large amounts of chlorobenzene in Cu(II) or Ni(II)-catalysed oxidations of alkanes in ACN or DCM media.[50,52] Chlorobenzene is formed through the decarboxylation of the ArC(O)O• radical with the subsequent abstraction of the H-atom by the Ar• radical (Scheme 3). In turn, the ArC(O)O• radical is generated *via* the homolytic splitting of the O–O bond of *m*CPBA.[48,49] The low amount of the chlorobenzene by-product in the case of the [**CuL**^{7}]/*m*CPBA system indicates either the reaction of the ArC(O)O• radical with the substrate prior to its decarboxylation or heterolytic splitting of the oxidant. Since the latter pathway is not favourable for Cu(II) complexes which do not form stable high-valent copper-oxo species, fast consumption of the ArC(O)O• radical upon reaction with the alkane could be an explanation. Other details including the evolution of the optical spectra of [**CuL**^{7}] in the presence of *m*CPBA and different substrates and the GC chromatograms of different substrates can be seen in Fig. S32–S35.†

Computational study of the catalytic reaction mechanism. Experimental data demonstrated that [**CuL**^{7}] acts as an efficient (pre)catalyst in the solvent-free oxidation of alkanes with ^{t}BuOOH (TBPH) or *m*CPBA as terminal oxidants. The selectivities and products in the cyclohexane (CyH) oxidation by ^{t}BuOOH catalysed by [**CuL**^{7}] indicated that ^{t}BuO• radicals act as the H-abstracting species. ^{t}BuOOH can produce two kinds of O-centred radicals, ^{t}BuOO• and ^{t}BuO•, both capable of reacting with CyH. The $\Delta G^{\ddagger}$ barriers for these reactions are 26.3 and 14.9 kcal mol^{-1}, respectively (Table S5†). For bimolecular first-order reactions, this $\Delta\Delta G^{\ddagger}$ difference of 11.4 kcal mol^{-1} corresponds to 10^7 times the difference in rate constants according to the Eyring equation. Although the true difference between these reaction rates should be smaller due to the idealised conditions as well as the large excess of the substrate (cyclohexane) under solvent-free conditions, these barriers suggest that ^{t}BuO• is the likely H-attacking radical. The energy of the catalyst-free splitting of the O–O bond of ^{t}BuOOH was studied at the BHLYP/def2-TZVP level (see the Experimental section for details). The respective minimum energy crossing point (MECP) was assigned to d(O–O) = 1.898 Å with a ΔG^{MECP} of no less than 36.8 kcal mol^{-1} at 50 °C (Table S6†), indicating that the spontaneous splitting of the ^{t}BuOOH O–O bond is not favourable. This conclusion agrees with the absence of back-
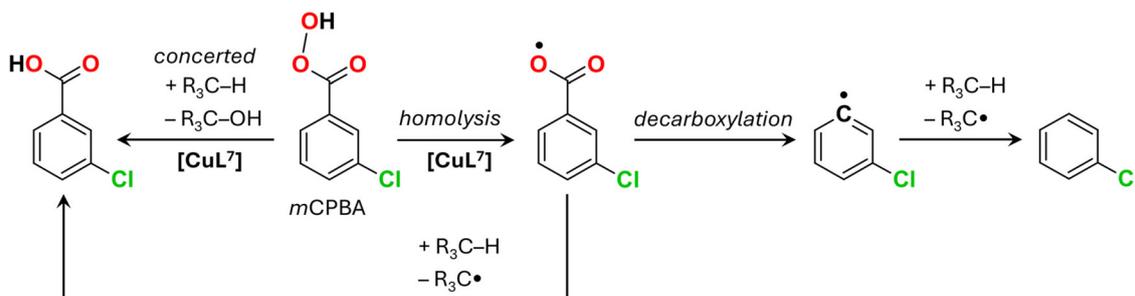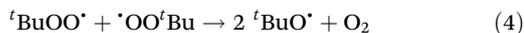

Scheme 3 General representation of the *m*CPBA reaction pathways and products.

ground catalyst-free cyclohexane oxidation under the conditions of the experiment.

The large size of the molecule of [**CuL**[7]], augmented with the oxidant and/or substrate binding, excluded the possibility of the use of a PBE0/def2-TZVP level of theory for the calculation of the vibrational energy. Hence, the composite DFT method B97-3c was applied,[53] which is among the lightest methods producing reliable geometries and frequencies.[54] The electronic energies of the optimised structures were recalculated at the PBE0/def2-TZVPP level. It should however be stressed that even at this level, the search for the transition states was not computationally feasible. Therefore, the current study is focused on the stable intermediates (IMs) only. The interaction of TBHP (^{t}BuOOH) with a Cu(II) or Cu(I) catalyst under aerobic conditions is known to proceed through the following general steps (1)–(4). The experimental observation of di-*tert*-butylhydroperoxide (Fig. S26†) agrees with reaction (3), while its direct formation from the coupling of two ^{t}BuO$^•$ radicals is not likely due to the large excess of the substrate (cyclohexane), which quickly consumes these radicals.

$$^t\text{BuOOH} + \text{Cu}^{II} \rightarrow {^t\text{BuOO}^•} + \text{Cu}^{I} + \text{H}^+ \tag{1}$$

$$^t\text{BuOOH} + \text{Cu}^{I} + \text{H}^+ \rightarrow {^t\text{BuO}^•} + \text{Cu}^{II} + \text{H}_2\text{O} \tag{2}$$

$$^t\text{BuOO}^• + {^•\text{OO}^t\text{Bu}} \rightarrow {^t\text{BuOO}^t\text{Bu}} \tag{3}$$

$$^t\text{BuOO}^• + {^•\text{OO}^t\text{Bu}} \rightarrow 2\ {^t\text{BuO}^•} + \text{O}_2 \tag{4}$$

Optimisation of the {[**CuL**[7]]·TBHP} intermediate ^{2}**IM1** with the TBHP molecule docked close to the apical position of copper(II) led to several possible configurations. The high flexibility of the [**CuL**[7]] molecule as well as of its assemblies with the oxidant explains the significant discrepancies in the obtained Gibbs energies, as a small change in geometry results in several units of Gibbs energy change. The selected {[**CuL**[7]]·^{t}BuOOH} intermediate structure (^{2}**IM2**) has a free Gibbs energy of 5.0 kcal mol^{-1} above the sum of the separated components ([**CuL**[7]] + ^{t}BuOOH) and shows weak Cu···O interaction as evidenced by the long Cu···O distance of 2.877 Å with the electron density $\rho(r_{BCP})$ at the respective bond critical point of 0.014 a.u. (Fig. S36†).

Given that the reaction proceeds in an aprotic medium (cyclohexane), the proton released in reaction (1) was presumed to remain in the catalyst structure. The respective reduced and protonated complex ^{1}[**CuHL**[7]] has several possible configurations, ^{1}**IM2a**, ^{1}**IM2b**, and ^{1}**IM2c** (Fig. S37†). The intermediates ^{1}**IM2a** and ^{1}**IM2b** showed distorted tetrahedral geometries around the Cu(I) centre with Cu–OH bond lengths of 2.406 and 2.494 Å, respectively. The principal difference between ^{1}**IM2a** and ^{1}**IM2b** is in the ligand geometry which has a "twisted" form in the case of ^{1}**IM2b**. The $\Delta\Delta G$ difference between these two molecules is negligible (^{1}**IM2b** is 0.7 kcal mol^{-1} more stable). In contrast, the ^{1}**IM2c** structure features a dissociated hydroxyl group with $d(\text{Cu···O}) = 3.105$ Å, where the H-atom forms a hydrogen bond with one of the N-atoms (Fig. S37†). The Cu(I) atom adopts a trigonal-planar coordi-

nation geometry. The free Gibbs energy of ^{1}**IM2c** is 6.7 kcal mol^{-1} higher than that of ^{1}**IM2b**. Since the topologies of ^{1}**IM2a** and ^{1}**IM2b** are equal and the energies are close, one can presume fast interconversion of these two forms in solution.

As reaction (1) assumes the elimination of the ^{t}BuOO$^•$ radical, the search for the respective {^{1}[**CuHL**[7]]·^{t}BuOO$^•$} intermediate was performed. The interaction of the ^{t}BuOO$^•$ radical with ^{1}**IM2a** results in the oxidation of copper(I), H-transfer, and subsequent return to the starting ^{2}**IM1** assembly {[**CuL**[7]]·^{t}BuOOH}, revealing the insufficient resistance of ^{1}**IM2a** towards such an attack. The "twisted" intermediate ^{1}**IM2b** (Fig. S37†) forms a stable assembly {^{1}[**CuHL**[7]]·^{t}BuOO$^•$} where the ^{t}BuOO· radical is docked between the ligand groups (intermediate ^{2}**IM3b**, Fig. S38†) and the copper ion maintains its +1 oxidation state. The $\Delta\Delta G(^2$**IM3b**–^{2}**IM1**) difference of 32.5 kcal mol^{-1} (37.5 kcal mol^{-1} relative to the starting components ^{t}BuOOH + ^{1}[**CuHL**[7]]) indicates that this pathway of H-abstraction from ^{t}BuOOH is possible, but not a favourable one. As the reduced catalyst should then interact with a second ^{t}BuOOH molecule (reaction (2)), the respective intermediate {^{1}[**CuHL**[7]]·^{t}BuOOH} was modelled (^{1}**IM4b**, Fig. S38†). However, it was found to have a high ΔG of 41.9 kcal mol^{-1} relative to the starting components. Hence, the favourable pathway implies that the "twisted" form ^{1}**IM2b** is converted first to ^{1}**IM2a**, in which copper(I) is less sterically hindered (Fig. S37†). The participation of ^{1}**IM2a** could be possible if one considers the reaction of a second molecule of ^{t}BuOOH with the starting assembly ^{2}**IM2a**, {[**CuL**[7]]·^{t}BuOOH}, at the moment of release of the ^{t}BuOO$^•$ radical from it. In this way, the intermediate ^{1}**IM3a** is generated (Fig. 10), in which the ^{t}BuOOH molecule forms a bifurcated H-bond with the phenolato oxygen atoms of the Cu(I) catalyst species. This kind of oxidant substitution results in a ΔG change of −1.0 kcal mol^{-1} (Fig. 10). The final reoxidation of Cu(I) and decomposition of ^{1}**IM3a** into ^{2}**IM1**, H$_2$O and ^{t}BuO$^•$ lead to a final ΔG of −10.3 kcal mol^{-1}.

Modelling of the interaction of ^{t}BuOO$^•$ with the intermediate ^{1}**IM2c** (Fig. S37†) showed the formation of a species where the ^{t}BuOO$^•$ radical is coordinated to copper (intermediate ^{2}**IM3c**, Fig. S39†). Löwdin analysis reveals a 0.5708 spin population on the copper atom, which suggests its formal +2 oxidation state. The spin density of ^{2}**IM3c** is clearly distributed over the Cu(II) as well as the oxygen atoms of the coordinated peroxide (Fig. S39†). Remarkably, the free Gibbs energy of ^{2}**IM3c** is considerably smaller than that of ^{2}**IM3b**, with $\Delta\Delta G(^2$**IM3c**–^{2}**IM1**) = 19.7 kcal mol^{-1} (Fig. S40†). The disassembly of ^{2}**IM3c** into the reduced complex ^{1}[**CuHL**[7]] (intermediate ^{1}**IM2c**) and the free ^{t}BuOO$^•$ radical shows a further increase in free Gibbs energy by 13.0 kcal mol^{-1} (overall $\Delta\Delta G$ of 37.7 kcal mol^{-1} relative to the sum of the starting components). This increase in the energy can be avoided if one considers the reaction of ^{t}BuOOH with the ^{2}**IM3c** intermediate and replacement of the ^{t}BuOO$^•$ radical with the ^{t}BuOOH molecule (intermediate ^{1}**IM4c**, Fig. S38†), which has $\Delta\Delta G(^1$**IM4c**–^{2}**IM3c**) = 6.8 kcal mol^{-1} and $\Delta\Delta G(^1$**IM4c**–^{2}**IM1**) = 25.9 kcal mol^{-1}.

Since the ligand in [**CuL**[7]] was shown to participate in the redox processes, the possibility of ligand oxidation during the
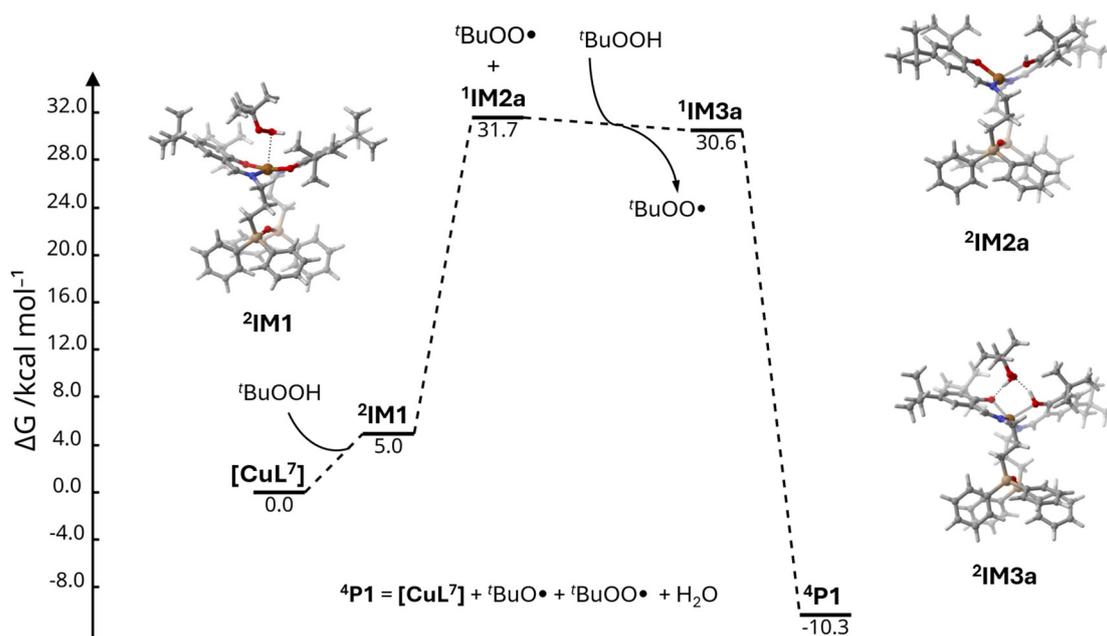
Fig. 10 Molecular structures and relative free Gibbs energies (kcal mol^{-1}) of the reaction between [**CuL^7**] and the ^{t}BuOOH oxidant.

catalytic process was assessed. Modelling of the direct homolytic splitting of the O–O bond of ^{t}BuOOH in ^{2}**IM1** resulted in the configuration ^{4}**IM2d** with the Cu–OH entity (Fig. S41†) and interatomic separation d(Cu–O) = 1.999 Å. The analysis of the spin density revealed that the eliminated species is a ^{t}BuO$^\bullet$ radical, and most of the other spin densities concentrated on both the phenoxyl group and one of the phenolic rings of the coordinated ligand. The overall ΔG of ^{4}**IM2d** is too high (41.4 kcal mol^{-1} relative to the starting components) for this pathway to be considered as a likely one.

In contrast to the [**CuL^7**]/TBHP catalytic system, the UV–vis spectra of [**CuL^7**]/*m*CPBA solutions in cyclohexane reveal fast degradation of the complex as evidenced by the disappearance of the characteristic absorption bands at 327 and 382 nm (Fig. S32 and S33†). This result is associated with *m*CPBA only, since the treatment of [**CuL^7**] with *m*-chlorobenzoic acid (*m*CBA) in cyclohexane at 50 °C does not afford degradation of the compound.

The non-catalytic decomposition of *m*CPBA is known to be rather complex[49] and may involve numerous organic radicals, from which the most principal ones are Ar$^\bullet$, ArC(O)O$^\bullet$ and ArC(O)OO$^\bullet$. The calculated energy barriers of H-abstraction from cyclohexane at 50 °C are 10.9, 9.8 and 21.2 kcal mol^{-1}, respectively (Table S5†), indicating that aryl and aroyloxyl radicals readily react with cyclohexane, while the aroylperoxyl one is less active. The energy barrier of the decarboxylation of ArC(O)O$^\bullet$ was estimated to be 8.6 kcal mol^{-1} (Table S5†). The experimental catalytic selectivity data agree with the involvement of aroyloxyl radicals. Since the latter can be formed through the direct decomposition of *m*CPBA, the energy of its O–O bond splitting was studied. The respective MECP point is approximately 39.1 kcal mol^{-1} higher than the energy of a singlet state

of *m*CPBA (Table S6†), suggesting that the catalyst-free decomposition of *m*CPBA should be negligible, in agreement with the experimental data.

Similarly to TBPH, the interaction between complex [**CuL^7**] and *m*CPBA produced several plausible configurations, where the *m*CPBA molecule is located parallel to one of the phenyl groups of the ligand or coordinated to the Cu(ɪɪ) atom. The kind of the starting configuration determines the further reaction pathway. The intermediate ^{2}**IM1e** formed by the non-covalent interaction of [**CuL^7**] and *m*CPBA has a free Gibbs energy by 8.0 kcal mol^{-1} higher than the sum of the energies of the starting components (Fig. 11). It is commonly assumed that the homolytic splitting of the O–O bond of *m*CPBA required for the elimination of the ArC(O)O$^\bullet$ radical coordinated to a metal centre M^n results either in the increase of its oxidation state (M^{n+1}) or in the formation of the oxyl species M^n=O$^\bullet$.[50] In the present case, splitting of the O–O bond produced a stable intermediate ^{4}**IM2e** featuring a Cu–OH entity with d(Cu–O) = 1.980 Å and the ArC(O)O$^\bullet$ radical located in close proximity (Fig. 11). Analysis of the spin density clearly indicates the oxidation of one of the phenolato groups of the coordinated ligand to a phenoxyl radical (Fig. S42†). Remarkably, the relative energy of the intermediate ^{4}**IM2e** of $\Delta\Delta G$(^{4}**IM2e**–^{2}**IM1e**) = 19.2 kcal mol^{-1} suggests that this step is possible. Further decomposition of the intermediate ^{4}**IM2e** into the oxidised species ^{3}[**Cu(OH)L^7**] (intermediate ^{3}**IM3e**) and release of the ArC(O)O$^\bullet$ radical afforded a slight increase in the energy by 6.6 kcal mol^{-1}. Replacement of the ArC(O)O$^\bullet$ radical in ^{4}**IM2e** by an *m*CPBA molecule produced the intermediate ^{3}**IM4e**, whose energy is 4.3 kcal mol^{-1} higher than that of ^{4}**IM2e** (Fig. 11). Note that H-transfer of the proton from *m*CPBA to the coordinated OH group proceeded with a huge −40.1 kcal mol^{-1} drop of the free Gibbs energy down to −8.6 kcal

Fig. 11 Molecular structures and relative free Gibbs energies (kcal mol^{-1}) of the reaction between [CuL^7] and the mCPBA oxidant, route (e).

mol^{-1} relative to the starting energy sum of [CuL^7] and 2 mCPBA molecules (intermediate ^{3}IM5e).

Optimisation of the complex [CuL^7] with an approaching water molecule led to the decoordination of the latter from the copper centre. Hence, the release of the ArC(O)OO$^{\bullet}$ radical from the intermediate ^{3}IM5e should regenerate the initial [CuL^7] structure and release a free water molecule. The overall energies of the intermediates (Fig. 11) suggest that this pathway is feasible.

The search for an intermediate with mCPBA coordinated to the Cu(II) centre in [CuL^7] gave rise to the structure ^{2}IM1f, where the phenolato group is protonated and dissociated, while the deprotonated mCPBA acts as a bidentate chelating co-ligand (Fig. 12). Splitting of the O–O bond in the intermediate ^{2}IM1f is followed by the complete dissociation of one N,O-donor Schiff base chelating group (intermediate ^{4}IM2f). Surprisingly, the analysis of the spin density indicated a doubly oxidised ligand, while the coordinated m-chlorobenzo-
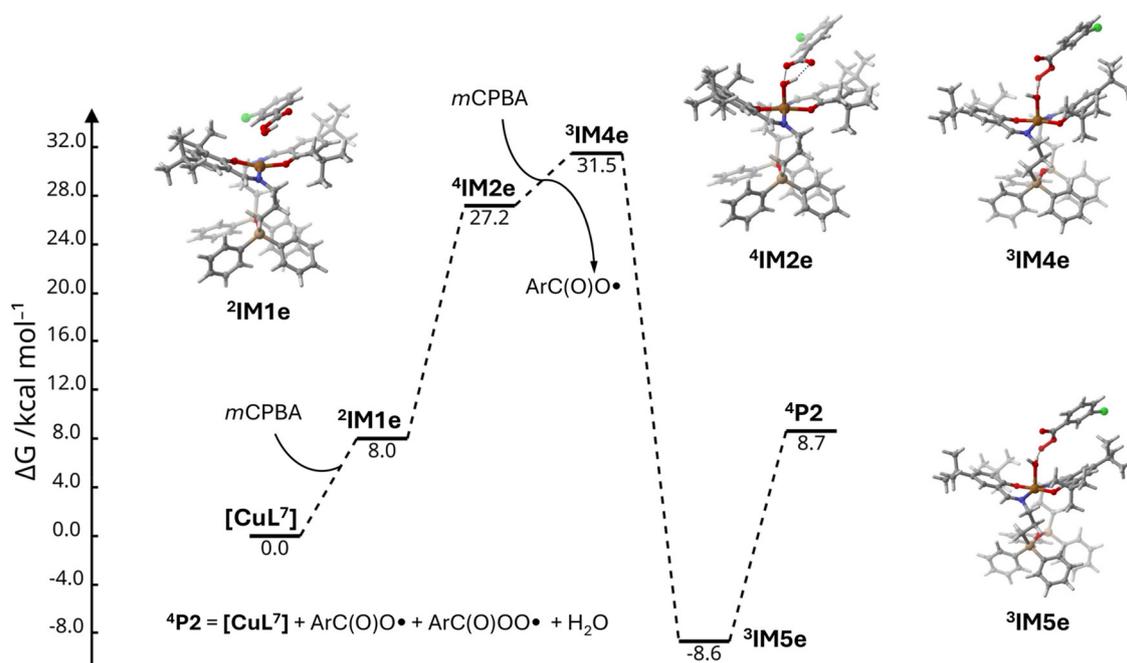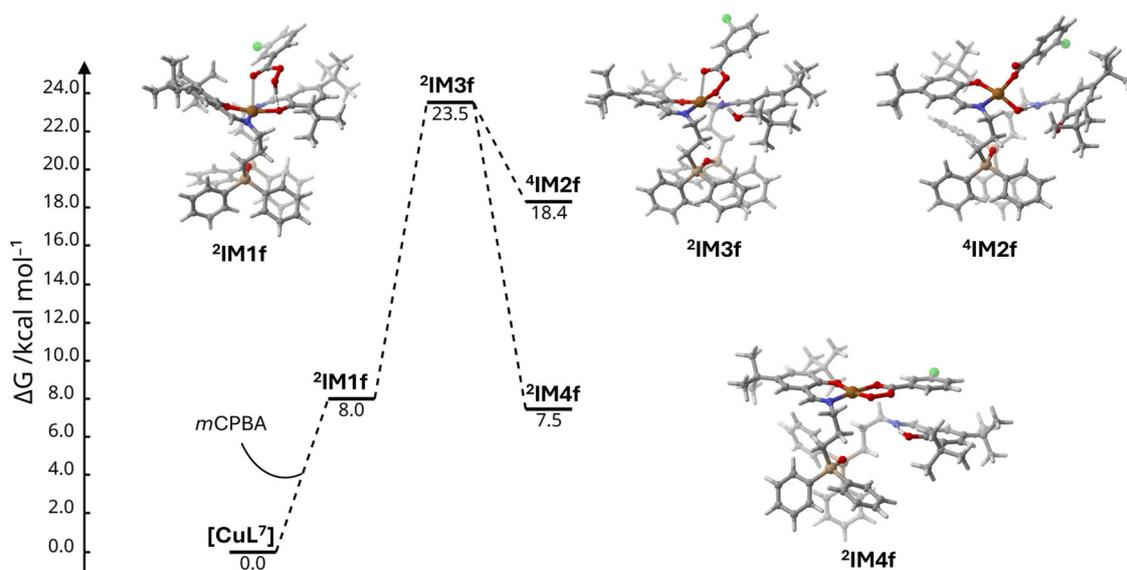

Fig. 12 Molecular structures and relative free Gibbs energies (kcal mol^{-1}) of the reaction between [CuL^7] and the mCPBA oxidant, route (f).

ate holds no unpaired electrons (Fig. S42†). The energy of ^{4}**IM2f** is rather low (18.3 kcal mol^{-1} relative to the starting components). If no O–O bond splitting is assumed, the intermediate ^{2}**IM1f** converts into the ^{2}**IM3f** species, where the protonated half of the Schiff base ligand is decoordinated moving further apart, while the mCPBA peroxycarboxylate replaces the dissociated part of the ligand in the coordination sphere (Fig. 12). Finally, the peroxycarboxylate residue shifts to form a square-planar intermediate ^{2}**IM4f**. All the intermediates ^{4}**IM2f**, ^{2}**IM3f** and ^{2}**IM4f** stipulate degradation of the starting catalyst [**CuL^7**] because decoordination of m-chlorobenzoate in ^{4}**IM2f** seems to be not likely in the presence of excess mCPBA and mCBA which should react with the oxidised ligand and further replace it in the coordination sphere of copper. The fate of the intermediates ^{2}**IM3f** and ^{2}**IM4f** is expected to be a step-by-step formation of the [Cu(mCBA)$_2$] species, achieved through the protonation and replacement of the second Schiff base group. One can presume that [Cu(mCBA)$_2$] undergoes dimerisation to form a quite stable paddlewheel carboxylate complex [Cu$_2$(mCBA)$_4$], which is responsible for further catalytic activity. Moreover, the UV–vis spectrum of the adduct of [Cu$_2$(mCBA)$_4$] with acetonitrile is reported[55] to be similar to that observed after degradation of the [**CuL^7**]/mCPBA catalytic system (Fig. S32†) and after dissolving metallic copper in a cyclohexane solution of mCPBA (Fig. S34†).

The stability of [**CuL^7**] in the presence of m-chlorobenzoic acid (mCBA), in contrast to mCPBA, can be rationalised in terms of the absence of numerous intermediate states (^{2}**IM1f**, ^{2}**IM3f** and ^{2}**IM4f**). Optimisation of the {[**CuL^7**]·mCBA} assemblies does not afford monodentate coordination of m-chlorobenzoate but shows the starting approach of mCBA (^{2}**IM1g**) and complete dissociation of the protonated bidentate Schiff base ligand (^{2}**IM2g**, Fig. S43†). Thus, although the overall process is energetically favourable, it may have sufficiently high barriers to prevent the rapid decomposition of [**CuL^7**] by mCBA.

Conclusion

In this work, we aimed at the synthesis of a Cu(II) complex soluble in non-polar solvents and studied its potential to act as a catalyst in the oxidation of cyclohexane used both as the substrate and the solvent. Our previous studies on the synthesis and catalytic activity of copper(II) complexes with quite unusual Schiff bases derived from substituted 2-hydroxybenzaldehydes and 1,3-bis(3-aminopropyl)tetramethyldisiloxane (**H$_2$L^1**–**H$_2$L^6**) prompted us to develop the synthesis of a similar Schiff base, in which the central tetramethyldisiloxane unit is replaced by a more lipophilic tetraphenyldisiloxane moiety. We performed a seven-step synthesis of a new Schiff base **H$_2$L^7** resulting finally from the condensation reaction of the commercially unavailable 1,3-bis(3-aminopropyl)tetraphenyldisiloxane as a diformate salt and 3,5-di-$tert$-butyl-2-hydroxybenzaldehyde in the presence of a base. The Cu(II) complex [**CuL^7**] obtained by the reaction of **H$_2$L^7** with Cu(OAc)$_2$ has a see-saw

or sawhorse coordination geometry, as established by SC-XRD. This was also the case for [**CuL^1**]–[**CuL^6**] reported previously, with comparable τ_4-parameters of 0.420 and 0.372 for the two crystallographically independent molecules of [**CuL^7**]. The optical spectrum of [**CuL^7**] showed three intense absorption bands at 275, 327 and 380 nm due to π–π* and LMCT σ–d transitions according to TDDFT calculations and weak absorption bands between 550 and 750 nm due to d–d transitions. Two consecutive one-electron reversible electrochemical oxidations were accompanied by a decrease in absorptions in the UV region of the optical spectrum of [**CuL^7**] and the simultaneous appearance and further development of a band at 304 nm due to the formation of phenoxyl mono- and di-radicals, respectively. Three new absorption bands appeared in the vis–NIR region of the optical spectrum at 530, 880 and 1500 nm. The DFT calculations have shown that the one-electron oxidised Cu(II) complex should exist in the triplet ground state as ^{3}[**CuL^7**]$^+$ with one unpaired electron located on the d$_{x^2-y^2}$ orbital of Cu(II) (d^9, $S = \frac{1}{2}$) and another unpaired electron located on the MO including p$_z$ orbitals of oxygen and carbon atoms of the phenoxyl moiety. Strong ferromagnetic interaction with coupling constant $J = 251.83$ cm^{-1} is predicted, even though the ferromagnetic ground state $S = 1$ remains to be confirmed experimentally. In turn, the doubly oxidised species [**CuL^7**]$^{2+}$ showed very close doublet and quartet states. The doublet state has an unpaired electron on the Cu(II) d-orbital, whereas the quartet state accommodates one unpaired electron on the Cu(II) d-orbital and two unpaired electrons on the ligand. Thus, spectroscopic and theoretical data clearly demonstrated the noninnocent behaviour of the coordinated Schiff base bearing the tetraphenyldisiloxane unit. Finally, [**CuL^7**] was found to act as a catalyst for the oxidation of cyclohexane to cyclohexanol and cyclohexanone under solvent-free conditions with hydrogen peroxide and $tert$-butyl hydroperoxide. Oxidation of cyclohexane with m-chloroperoxybenzoic acid in the presence of the Cu(II) complex resulted in cyclohexanol (29.1%), cyclohexene oxide (3.0%) and ε-caprolactone (29.8%) relative to mCPBA. DFT theoretical investigations of the reaction mechanism disclosed principal intermediates formed upon the reaction of [**CuL^7**] with organic peroxides, where participation of the noninnocent ligand in the redox processes is among the possible reaction pathways.

Experimental section

The multistep synthesis of the diammonium formate salt **G** is described in the ESI.†

Synthesis of the Schiff base and Cu(II) complex

H$_2$L^7·0.75H$_2$O. To a solution of species **G** (300.5 mg, 0.51 mmol) in methanol (6 mL), triethylamine (149.2 μL, 1.07 mmol) and 3,5-di-$tert$-butyl-2-hydroxybenzaldehyde (251 mg, 1.07 mmol) were added. The suspension was stirred at reflux for 3 h. After cooling to room temperature, the sus-

pension was diluted with DCM (20 mL) and bound to silica. The crude product was purified on silica using hexane : ethylacetate 9 : 1 as an eluent to give a yellow solid after drying at 50 °C *in vacuo* overnight. Yield: 394.2 mg, 83%. ^{1}H NMR (600 MHz, DMSO-d_6), δ, ppm: 14.10 (s, 1H, H^{20}), 8.35 (s, 1H, H^{13}), 7.46 (dd, J = 7.9, 1.3 Hz, 4H, H^2, H^6), 7.37–7.33 (m, 2H, H^4, H^8), 7.29 (dd, J = 12.7, 4.9 Hz, 5H, H^{17}, H^3, H^7), 7.19 (d, J = 2.4 Hz, 1H, H^{19}), 3.42 (t, J = 6.4 Hz, 2H, H^{11}), 1.60–1.53 (m, 2H, H^{10}), 1.37 (s, 9H, H^{22}), 1.25 (s, 9H, H^{24}), 1.15–1.10 (m, 2H, H^9). ^{13}C NMR (151 MHz, DMSO-d_6) δ, ppm: 166.78 (CH, C^{13}), 157.85 (Cq, C^{15}), 139.29 (Cq, C^{18}), 135.71 (Cq, C^1, C^5), 135.59 (Cq, C^{16}), 133.72 (CH, C^2, C^6), 129.84 (CH, C^4, C^8), 127.88 (CH, C^3, C^7), 126.13 (CH, C^{19}), 126.00 (CH, C^{17}), 117.57 (Cq, C^{14}), 60.62 (CH$_2$, C^{11}), 34.55 (Cq, C^{21}), 33.80 (Cq, C^{23}), 31.26 (CH$_3$, C^{24}), 29.15 (CH$_3$, C^{22}), 24.41 (CH$_2$, C^{10}), 12.29 (CH$_2$, C^9). ^{29}Si NMR (119 MHz, DMSO-d_6) δ, ppm: −10.35 (s). ESI-MS (acetonitrile/methanol + 1% water), positive: m/z 929.62 [M + H$^+$]$^+$ (calcd m/z for $[C_{60}H_{77}N_2O_3Si_2]^+$ 929.55). Anal. calcd for $C_{60}H_{76}N_3O_3Si_2 \cdot 0.75H_2O$ (M_r = 942.94), %: C, 76.43; H, 8.28; N, 2.97. Found, %: C, 76.33; H, 8.13; N, 3.06.

CuL^7·0.3CHCl$_3$. To a solution of H$_2$L^7 (59 mg, 0.064 mmol) in chloroform (1 mL), a solution of Cu(OAc)$_2$·H$_2$O (13 mg, 0.064 mmol) in methanol (1.3 mL) was added. The dark-green solution was stirred at reflux for 30 min and subsequently cooled to room temperature. The solvent was slowly evaporated producing dark-green crystals. These crystals were further stored at room temperature for 24 h and found to be of X-ray diffraction quality. Several crystals were selected for SC-XRD measurement, while the main portion was filtered off and dried *in vacuo* for 24 h. Yield: 52 mg, 83%. ESI-MS (acetonitrile/methanol + 1% water), positive: m/z 990.53 [M + H$^+$]$^+$ (calcd m/z for $[C_{60}H_{75}CuN_2O_3Si_2]^+$ 990.47). Anal. calcd for $C_{60}H_{74}CuN_3O_3Si_2 \cdot 0.3CHCl_3$ (M_r = 1026.77), %: C, 70.53; H, 7.29; N, 2.72. Found, %: C, 70.22; H, 7.36; N, 2.82.

Physical measurements. Elemental analysis was carried out with a Carlo-Erba microanalyzer at the Microanalytical Laboratory of the Faculty of Chemistry, University of Vienna. The samples for electrospray ionisation mass spectrometry (ESI-MS) were measured on an Amazon speed ETD Bruker instrument. Expected and experimental isotope distributions were compared. UV–vis spectra were recorded using a PerkinElmer Lambda 35 spectrometer in the 200–1000 nm spectral range using quartz cuvettes (10 mm; Labbox SMSQ-010-002). Since commercial hydrocarbon substrates were used as solvents and may contain admixtures in small amounts, their purity was verified by gas chromatography (Fig. S35†). 1D (^{1}H, ^{13}C) and 2D (^{1}H–^{1}H COSY, ^{1}H–^{13}C HSQC, ^{1}H–^{13}C HMBC) NMR spectra were acquired on a Bruker AV NEO 500 or AV III 600 spectrometer in DMSO-d_6 at 25 °C.

Crystallographic structure determination. X-ray diffraction measurements of diol **D** and **CuL^7** were performed on an STOE Stadivari diffractometer. Single crystals were positioned at 40 and 80 mm from the detector, and 1721 and 5070 frames were measured, each for 4 and 10 s over 0.5° scan width, respectively. Crystal data, data collection parameters, and structure refinement details are given in Table S1.† The structures were solved by direct methods and refined by full-matrix least-squares techniques. Non-H atoms were refined with anisotropic displacement parameters. H atoms were inserted in calculated positions and refined with a riding model. The disorder of interstitial solvent in the voids of **CuL^7** could be resolved by using SADI, EADP and ISOR restraints, and the volume of the voids per unit cell (666.9 Å^3) was determined by using the SQUEEZE routine implemented in PLATON.[56] The following computer programs and hardware were used: structure solution, *SHELXS-2014*; refinement, *SHELXL-2014*;[57] molecular diagrams, *ORTEP*;[58] and computer, Intel CoreDuo. CCDC no.: 2413535 (diol D) and 2413536 (**CuL^7**).†

Electrochemistry and spectroelectrochemistry. The cyclic voltammograms (CVs) were recorded in a 0.1 M solution of tetrabutylammonium hexafluorophosphate (nBu$_4$NPF$_6$, puriss quality from Fluka) as a supporting electrolyte in DCM using a single-compartment electrochemical cell with a working glassy-carbon GC-disk electrode (from Ionode, Australia), a platinum wire as the counter electrode, and a silver wire as a pseudoreference electrode at a scan rate of 100 mV s$^{−1}$. All potentials in voltammetric studies were quoted *vs.* the ferricenium/ferrocene (Fc$^+$/Fc) redox couple (purchased from Sigma Aldrich). A Heka PG310USB potentiostat (Lambrecht, Germany) with the PotMaster 2.73 software package was used for potential control in the voltammetric studies. EPR measurements were performed using an X-band Bruker EMX spectrometer (Germany). Standard settings used during EPR spectroelectrochemical experiments were as follows: microwave frequency ~9.795 GHz; power of the microwave radiation 10 mW; sweep width 700 G; centre field 3400 G; modulation amplitude 2 G; time constant 41 ms; sweep time 42 s; and 1 scan for each measurement. Optical spectra in dichloromethane (SeccoSolv max. 0.025% H$_2$O, Merck) were recorded on a Shimadzu 3600 UV–vis–NIR spectrometer (Japan) in a quartz cuvette, with an optical path length of 10 mm. Spectroelectrochemical studies were performed on a UV–vis–NIR Avantes spectrometer (Model AvaSpec-2048_14-USB2).

Catalytic solvent-free oxidation of alkanes. Unless stated otherwise, 8.5 mg (5 μmol) of the catalyst was added into a thermostated reaction vessel. Then, liquid alkane was added with the subsequent addition of a liquid oxidant (0.28 mL of H$_2$O$_2$, 50% aq. or 0.69 mL of TBHP, 70% aq.) to obtain a total reaction volume of 5 mL. In the case of the *m*CPBA oxidant, 0.11 mg (0.5 mmol) of solid *m*CPBA (77%) was weighed into the reaction vessel before the addition of the alkane. The latter was added with immediate vigorous stirring. The reaction vessel was kept under stirring at 50 °C for 24 h. After cooling the reaction vessel, an aliquot (1 mL) of the reaction mixture was mixed with an equal volume of ethylacetate solution of the internal standard, cyclooctanone (*ca.* 50 μM). The resulting mixture was transferred into a vial containing an excess of solid PPh$_3$ (according to the method developed by Shul'pin). After the completion of the reduction reaction (*ca.* 30 min), the mixture was analysed directly by gas chromatography GC/GC-MS techniques.

Gas chromatography. A PerkinElmer Clarus 500 gas chromatograph (SGE BP-20 capillary GC column, 30 m × 0.22 mm

× 0.25 μm dimensions) equipped with a FID detector, and a PerkinElmer Clarus 600 gas chromatograph (two Phenomenex Zebron ZB-5 capillary GC columns, 30 m × 0.25 mm × 0.25 μm dimensions) equipped with a FID detector and a PerkinElmer Clarus 600 C electron impact mass spectrometer were used for quantitative and qualitative analyses of the catalytic mixtures (helium carrier gas was used). All electron ionisation (EI) mass spectra were recorded using 70 eV ionisation energy. The identification of the product peaks in the chromatograms was made on the basis of the NIST v. 2.2 mass spectral database (PerkinElmer TurboMass v. 5.4.2.1617 software was used). Unless stated otherwise, all the chromatograms depicted in Fig. S35† were recorded using low-polarity ZB-5 columns.

Theoretical calculations. The ORCA 6.0.0. and 6.0.1 packages[59–61] were used for all calculations. Unless stated otherwise, the PBE0 hybrid functional[62,63] with the def2-TZVP basis set[64] was used for geometry optimisations. Dispersion correction was introduced through the *D4* keyword (Grimme's atom-pairwise approach),[65] and the *AutoAux* keyword[66] was used to generate the auxiliary basis sets in all calculations. The SMD implicit solvation model[67] was used to account for solvation effects. The SCF convergence criteria were set using the *VeryTightSCF* keyword, and an integration grid of default density (*Defgrid2*) was employed. The step length and trust radius were adjusted by setting "*Maxstep 0.03*" and "*Trust −0.03*" to avoid oscillations during the final geometry optimisations of large molecules. The geometry convergence criteria were set using the keywords "*OPT*" and "*EnforceStrictConvergence true*" in all cases. In certain cases, single-point energies were calculated using the ωB97M-V functional[68] and the def2-QZVPP basis set.[64] For the reaction mechanism study, the composite B97-3c DFT method[53] was used in all cases for optimisation of structures and the calculation of vibrational frequencies. The thermochemical parameters were calculated at 323.15 K. Final single-point energies were calculated using the PBE0 functional and def2-TZVPP basis set involving D4 dispersion correction. The final Gibbs energies (G) were calculated as $G^{final} = G^{B97-3c} − E^{B97-3c} + E^{PBE0-D4/def2-TZVPP} + RT \ln V_m^0$ where E is the single-point energy. The last term (2.1 kcal mol^{-1}) is a correction[69] for the standard state to 1 M and 323.15 K. The search for minimum energy crossing points (MECP) was performed using the BHandLYP functional[70] and the def2-TZVP basis set, along with the D4 dispersion correction. To reduce the numerical noise and increase the stability, the integration grid of high density was used (*Defgrid3* keyword) along with the *ExtremeSCF* convergence criteria. Also, all the RI approximations were switched off by the *NORI* and *NoSplit-RI-J* keywords. The maximum step in the optimisation was limited by the "*Maxstep 0.01*" command. Finally, the starting guess for every SCF cycle was switched from the default "MORead" to "PModel" (command "*OptGuess = PModel*"). All these parameters were essential for achieving the MECP structures and avoiding spin contamination of the low-spin $S = 0$ state.

The broken symmetry calculations were done using the PBE0 functional and the def2-TZVPP basis set[64] for all atoms.

The TDDFT excited-state calculations, unless stated otherwise, were performed using the PBE0 functional and the DKH relativistic approximation,[71,72] employing the aug-cc-pVTZ-DK basis set for the copper atom and aug-cc-pVDZ-DK for all other atoms,[73,74] along with the SARC/J auxiliary basis set.[75,76] The Tamm–Dancoff approximation (TDA)[77] and Gaussian finite nucleus model[78] were applied for all TDDFT calculations, as well as the SMD implicit solvation model. In certain cases, the TDDFT calculations involved the ma-def2-SVP[79] or 6-311G*[80] basis sets and the B3LYP hybrid functional.[81–83] Natural transition orbitals[84] were used for visualisation of electronic transitions. The CASSCF/SC-NEVPT2 studies[85,86] were performed using the def2-TZVP basis set for copper and the N,O,C-atoms of the Schiff base ligands (excluding ^tBu groups) and def2-SVP[64] for all other atoms, employing *VeryTightSCF* convergence criteria and considering the SMD implicit solvation model. In certain cases, the Ab Initio Ligand Field Theory (AILFT) calculations[87] were involved in the CASSCF studies. The MC-RPA calculations[88] were performed using the same basis set combination as for the CASSCF studies. All calculations involved RIJ-COSX[89–91] (for DFT and MC-RPA) or RI[92] (for CASSCF) speed-up approximations. Visualisation of the molecular structures of intermediates, orbitals and spin densities was drawn using the CYLview20[93] and Avogadro 1.2 programs.[94] Free energy profile diagrams were drawn using the mechaSVG 0.1.1 program.[95] Unless stated otherwise, the isosurfaces of the molecular orbitals are shown at the 0.03 a.u. level and isosurfaces of spin densities at the 0.005 a.u. level. Selected ORCA inputs and outputs used for the calculations are provided in Listings S1–S8. The Cartesian *xyz* files provided in the ESI† contain the DFT-optimised structures.

Author contributions

Christopher Wittmann – formal analysis; investigation; and writing – original draft. Oleg Palamarciuc – investigation. Mihaela Dascalu – data curation and investigation. Maria Cazacu – writing – original draft; formal analysis; and methodology. Dmytro Nesterov – investigation; methodology; software; validation; and writing – review. Armando J. L. Pombeiro – conceptualisation and writing – review and editing. Peter Rapta – investigation; methodology; and writing – original draft. Vladimir B. Arion – conceptualisation; funding acquisition; investigation; project administration; and writing – review and editing.

Conflicts of interest

There are no conflicts to declare.

Data availability

The data supporting this article have been included as part of the ESI.†

Crystallographic data for compounds diol **D** and **CuL**[7] have been deposited at the CCDC under accession numbers 2413535 and 2413536† and can be obtained from CCDC e-mail: deposit@ccdc.cam.ac.uk.

Acknowledgements

References

1 M. Damoc, A.-C. Stoica, M. Dascalu, M. Asandulesa, S. Shova and M. Cazacu, *Dalton Trans.*, 2021, **50**, 13841–13858.

2 A. Soroceanu, M. Cazacu, S. Shova, C. Turta, J. Kožíšek, M. Gall, M. Breza, P. Rapta, T. C. O. Mac Leod, A. J. L. Pombeiro, J. Telser, A. A. Dobrov and V. B. Arion, *Eur. J. Inorg. Chem.*, 2013, 1458–1474.

3 M. Cazacu, S. Shova, A. Soroceanu, P. Machata, L. Bucinsky, M. Breza, P. Rapta, J. Telser, J. Krzystek and V. B. Arion, *Inorg. Chem.*, 2015, **54**, 5691–5706.

4 A. Vlad, M.-F. Zaltariov, S. Shova, M. Cazacu, M. Avadanei, A. Soroceanu and P. Samoila, *Polyhedron*, 2016, **115**, 76–85.

5 A. Vlad, M. Avadanei, S. Shova, M. Cazacu and M.-F. Zaltariov, *Polyhedron*, 2018, **146**, 129–135.

6 S. Shova, A. Vlad, M. Cazacu, J. Krzystek, L. Bucinsky, M. Breza, D. Darvasiová, P. Rapta, J. Cano, J. Telser and V. B. Arion, *Dalton Trans.*, 2017, **46**, 11817–11829.

7 M. Zaltariov, M. Alexandru, M. Cazacu, S. Shova, G. Novitchi, C. Train, A. Dobrov, M. V. Kirillova, E. C. B. A. Alegria, A. J. L. Pombeiro and V. B. Arion, *Eur. J. Inorg. Chem.*, 2014, 4946–4956.

8 M. Janeta, T. Lis and S. Szafert, *Chem. – Eur. J.*, 2020, **26**, 13686–13697.

9 B. A. Jazdzewski and W. B. Tolman, *Coord. Chem. Rev.*, 2000, **200–202**, 633–685.

10 S. Itoh, M. Taki and S. Fukuzumi, *Coord. Chem. Rev.*, 2000, **198**, 3–20.

11 C. T. Lyons and T. D. P. Stack, *Coord. Chem. Rev.*, 2013, **257**, 528–540.

12 E. Saint-Aman, S. Ménage, J.-L. Pierre, E. Defrancq and G. Gellon, *New J. Chem.*, 1998, **22**, 393–394.

13 A. K. Nairn, S. J. Archibald, R. Bhalla, B. C. Gilbert, E. J. MacLean, S. J. Teat and P. H. Walton, *Dalton Trans.*, 2006, 172–176.

14 K. Bernardo, S. Leppard, A. Robert, G. Commenges, F. Dahan and B. Meunier, *Inorg. Chem.*, 1996, **35**, 387–396.

15 L. Yang, D. R. Powell and R. P. Houser, *Dalton Trans.*, 2007, 955–964.

16 M. H. Reineke, M. D. Sampson, A. L. Rheingold and C. P. Kubiak, *Inorg. Chem.*, 2015, **54**, 3211–3217.

17 A. Okuniewski, D. Rosiak, J. Chojnacki and B. Becker, *Polyhedron*, 2015, **90**, 47–57.

18 T. Guchhait, M. Giri and S. P. Mishra, *J. Coord. Chem.*, 2024, **77**, 49–68.

19 T. Iwamoto, H. Masuda, S. Ishida, C. Kabuto and M. Kira, *J. Am. Chem. Soc.*, 2003, **125**, 9300–9301.

20 K. Kihara, *Eur. J. Mineral.*, 1990, **2**, 63–78.

21 C. Glidewell and D. C. Liles, *J. Chem. Soc., Chem. Commun.*, 1977, 632–633.

22 K. Suwińska, G. J. Palenik and R. Gerdil, *Acta Crystallogr., Sect. C: Cryst. Struct. Commun.*, 1986, **42**, 615–620.

23 C. Glidewell and D. C. Liles, *Acta Crystallogr., Sect. B*, 1978, **34**, 696–698.

24 M. A. Mazid and R. A. Palmer, *J. Cryst. Mol. Struct.*, 1975, **5**, 35–46.

25 P. K. Sahoo, S. S. Gawali and C. Gunanathan, *ACS Omega*, 2018, **3**, 124–136.

26 N. Kocher, J. Henn, B. Gostevskii, D. Kost, I. Kalikhman, B. Engels and D. Stalke, *J. Am. Chem. Soc.*, 2004, **126**, 5563–5568.

27 E. Bill, J. Müller, T. Weyhermüller and K. Wieghardt, *Inorg. Chem.*, 1999, **38**, 5795–5802.

28 T. Takeyama and Y. Shimazaki, *Dalton Trans.*, 2024, **53**, 3911–3929.

29 H. Kanso, R. M. Clarke, A. Kochem, H. Arora, C. Philouze, O. Jarjayes, T. Storr and F. Thomas, *Inorg. Chem.*, 2020, **59**, 5133–5148.

30 T. Takeyama, T. Suzuki, M. Kikuchi, M. Kobayashi, H. Oshita, K. Kawashima, S. Mori, H. Abe, N. Hoshino, S. Iwatsuki and Y. Shimazaki, *Eur. J. Inorg. Chem.*, 2021, 4133–4145.

31 T. Takeyama, M. Kobayashi, M. Kikuchi, T. Ogura, Y. Shimazaki and S. Iwatsuki, *Inorg. Chim. Acta*, 2020, **511**, 119848.

32 T. Storr, P. Verma, R. C. Pratt, E. C. Wasinger, Y. Shimazaki and T. D. P. Stack, *J. Am. Chem. Soc.*, 2008, **130**, 15448–15459.

33 P. Chaudhuri and K. Wieghardt, in *Progress in Inorganic Chemistry*, ed. K. D. Karlin, Wiley, 1st edn, 2001, vol. 50, pp. 151–216.

34 K. Asami, K. Tsukidate, S. Iwatsuki, F. Tani, S. Karasawa, L. Chiang, T. Storr, F. Thomas and Y. Shimazaki, *Inorg. Chem.*, 2012, **51**, 12450–12461.

35 D. De Bellefeuille, M. Orio, A.-L. Barra, A. Aukauloo, Y. Journaux, C. Philouze, X. Ottenwaelder and F. Thomas, *Inorg. Chem.*, 2015, **54**, 9013–9026.

36 M. Orio, O. Jarjayes, H. Kanso, C. Philouze, F. Neese and F. Thomas, *Angew. Chem., Int. Ed.*, 2010, **49**, 4989–4992.

37 J. Liang, X. Feng, D. Hait and M. Head-Gordon, *J. Chem. Theory Comput.*, 2022, **18**, 3460–3473.

38 O. V. Nesterova, O. Yu. Vassilyeva, B. W. Skelton, A. Bieńko, A. J. L. Pombeiro and D. S. Nesterov, *Dalton Trans.*, 2021, **50**, 14782–14796.

39 A. D. Laurent and D. Jacquemin, *Int. J. Quantum Chem.*, 2013, **113**, 2019–2039.

40 L. Chiang, K. Herasymchuk, F. Thomas and T. Storr, *Inorg. Chem.*, 2015, **54**, 5970–5980.

41 D. S. Nesterov, O. V. Nesterova and A. J. L. Pombeiro, *Coord. Chem. Rev.*, 2018, **355**, 199–222.

42 I. Gryca, K. Czerwińska, B. Machura, A. Chrobok, L. S. Shul'pina, M. L. Kuznetsov, D. S. Nesterov, Y. N. Kozlov, A. J. L. Pombeiro, I. A. Varyan and G. B. Shul'pin, *Inorg. Chem.*, 2018, **57**, 1824–1839.

43 O. V. Nesterova, D. S. Nesterov, A. Krogul-Sobczak, M. F. C. Guedes Da Silva and A. J. L. Pombeiro, *J. Mol. Catal. Chem.*, 2017, **426**, 506–515.

44 P. T. Wierzchowski and L. W. Zatorski, *Chromatographia*, 2000, **51**, 83–86.

45 Y. N. Kozlov, G. V. Nizova and G. B. Shul'pin, *Russ. J. Phys. Chem.*, 2001, **75**, 770–774.

46 G. B. Shul'pin, *Dalton Trans.*, 2013, **42**, 12794.

47 G. B. Shul'pin, *J. Mol. Catal. Chem.*, 2002, **189**, 39–66.

48 O. V. Nesterova, M. L. Kuznetsov, A. J. L. Pombeiro, G. B. Shul'pin and D. S. Nesterov, *Catal. Sci. Technol.*, 2022, **12**, 282–299.

49 A. Bravo, H.-R. Bjorsvik, F. Fontana, F. Minisci and A. Serri, *J. Org. Chem.*, 1996, **61**, 9409–9416.

50 D. S. Nesterov and O. V. Nesterova, *Catalysts*, 2021, **11**, 1148.

51 Y. Qiu and J. F. Hartwig, *J. Am. Chem. Soc.*, 2020, **142**, 19239–19248.

52 G. S. Astakhov, A. N. Bilyachenko, A. A. Korlyukov, M. M. Levitsky, L. S. Shul'pina, X. Bantreil, F. Lamaty, A. V. Vologzhanina, E. S. Shubina, P. V. Dorovatovskii, D. S. Nesterov, A. J. L. Pombeiro and G. B. Shul'pin, *Inorg. Chem.*, 2018, **57**, 11524–11529.

53 J. G. Brandenburg, C. Bannwarth, A. Hansen and S. Grimme, *J. Chem. Phys.*, 2018, **148**, 064104.

54 S. A. Katsyuba, E. E. Zvereva and S. Grimme, *J. Phys. Chem. A*, 2019, **123**, 3802–3808.

55 R. Kumar, A. Maji, B. Biswas and A. Draksharapu, *Dalton Trans.*, 2024, **53**, 5401–5406.

56 A. L. Spek, *J. Appl. Crystallogr.*, 2003, **36**, 7–13.

57 G. M. Sheldrick, *Acta Crystallogr., Sect. A: Found. Crystallogr.*, 2008, **64**, 112–122.

58 M. N. Burnett and C. K. Johnson, *ORTEP-III: Oak Ridge Thermal Ellipsoid Plot Program for crystal structure illustrations*, 1996.

59 F. Neese, *Wiley Interdiscip. Rev.: Comput. Mol. Sci.*, 2025, **15**, e70019.

60 F. Neese, F. Wennmohs, U. Becker and C. Riplinger, *J. Chem. Phys.*, 2020, **152**, 224108.

61 F. Neese, *J. Comput. Chem.*, 2023, **44**, 381–396.

62 C. Adamo and V. Barone, *J. Chem. Phys.*, 1999, **110**, 6158–6170.

63 M. Ernzerhof and G. E. Scuseria, *J. Chem. Phys.*, 1999, **110**, 5029–5036.

64 F. Weigend and R. Ahlrichs, *Phys. Chem. Chem. Phys.*, 2005, **7**, 3297–3305.

65 E. Caldeweyher, C. Bannwarth and S. Grimme, *J. Chem. Phys.*, 2017, **147**, 034112.

66 G. L. Stoychev, A. A. Auer and F. Neese, *J. Chem. Theory Comput.*, 2017, **13**, 554–562.

67 A. V. Marenich, C. J. Cramer and D. G. Truhlar, *J. Phys. Chem. B*, 2009, **113**, 6378–6396.

68 N. Mardirossian and M. Head-Gordon, *J. Chem. Phys.*, 2016, **144**, 214110.

69 J. N. Harvey, F. Himo, F. Maseras and L. Perrin, *ACS Catal.*, 2019, **9**, 6803–6813.

70 A. D. Becke, *J. Chem. Phys.*, 1993, **98**, 1372–1377.

71 B. A. Hess, *Phys. Rev. A*, 1985, **32**, 756–763.

72 M. Douglas and N. M. Kroll, *Ann. Phys.*, 1974, **82**, 89–155.

73 N. B. Balabanov and K. A. Peterson, *J. Chem. Phys.*, 2005, **123**, 064107.

74 K. A. Peterson and C. Puzzarini, *Theor. Chem. Acc.*, 2005, **114**, 283–296.

75 D. A. Pantazis and F. Neese, *Theor. Chem. Acc.*, 2012, **131**, 1292.

76 F. Weigend, *Phys. Chem. Chem. Phys.*, 2006, **8**, 1057–1065.

77 S. Hirata and M. Head-Gordon, *Chem. Phys. Lett.*, 1999, **314**, 291–299.

78 L. Visscher and K. G. Dyall, *At. Data Nucl. Data Tables*, 1997, **67**, 207–224.

79 J. Zheng, X. Xu and D. G. Truhlar, *Theor. Chem. Acc.*, 2011, **128**, 295–305.

80 R. Krishnan, J. S. Binkley, R. Seeger and J. A. Pople, *J. Chem. Phys.*, 1980, **72**, 650–654.

81 A. D. Becke, *J. Chem. Phys.*, 1993, **98**, 5648–5652.

82 C. Lee, W. Yang and R. G. Parr, *Phys. Rev. B: Condens. Matter Mater. Phys.*, 1988, **37**, 785–789.

83 R. H. Hertwig and W. Koch, *Chem. Phys. Lett.*, 1997, **268**, 345–351.

84 R. L. Martin, *J. Chem. Phys.*, 2003, **118**, 4775–4777.

85 C. Angeli, R. Cimiraglia, S. Evangelisti, T. Leininger and J.-P. Malrieu, *J. Chem. Phys.*, 2001, **114**, 10252–10264.

86 Y. Guo, K. Sivalingam and F. Neese, *J. Chem. Phys.*, 2021, **154**, 214111.

87 S. K. Singh, J. Eng, M. Atanasov and F. Neese, *Coord. Chem. Rev.*, 2017, **344**, 2–25.

88 B. Helmich-Paris, *J. Chem. Phys.*, 2019, **150**, 174121.

89 B. Helmich-Paris, B. De Souza, F. Neese and R. Izsák, *J. Chem. Phys.*, 2021, **155**, 104109.

90 F. Neese, F. Wennmohs, A. Hansen and U. Becker, *Chem. Phys.*, 2009, **356**, 98–109.

91 F. Neese, *J. Comput. Chem.*, 2003, **24**, 1740–1747.

92 F. Neese and G. Olbrich, *Chem. Phys. Lett.*, 2002, **362**, 170–178.

93 C. Y. Legault, *CYLview20*, Université de Sherbrooke, 2020.

94 M. D. Hanwell, D. E. Curtis, D. C. Lonie, T. Vandermeersch, E. Zurek and G. R. Hutchison, *J. Cheminf.*, 2012, **4**, 17.

95 R. A. Angnes, *ricalmang/mechaSVG v.0.0.8 (version v.0.0.8)*, Zenodo, 2020.